

THESIS

LASER DIAGNOSTIC METHOD FOR PLASMA SHEATH POTENTIAL MAPPING

Submitted by

Sean P. Walsh

Department of Mechanical Engineering

In partial fulfillment of the requirements

For the Degree of Master of Science

Colorado State University

Fort Collins, Colorado

Summer 2016

Master's Committee:

Advisor: Azer P. Yalin

John D. Williams

Jorge G. Rocca

Copyright by Sean P. Walsh 2016  
All Rights Reserved

## ABSTRACT

### LASER DIAGNOSTIC METHOD FOR PLASMA SHEATH POTENTIAL MAPPING

Electric propulsion systems are gaining popularity in the aerospace field as a viable option for long term positioning and thrusting applications. In particular, Hall thrusters have shown promise as the primary propulsion engine for space probes during interplanetary journeys. However, the interaction between propellant xenon ions and the ceramic channel wall continues to remain a complex issue. The most significant source of power loss in Hall thrusters is due to electron and ion currents through the sheath to the channel wall. A sheath is a region of high electric field that separates a plasma from a wall or surface in contact. Plasma electrons with enough energy to penetrate the sheath may result emission of a secondary electron from the wall. With significant secondary electron emission (SEE), the sheath voltage is reduced and so too is the electron retarding electric field. Therefore, a lower sheath voltage further increases the particle loss to the wall of a Hall thruster and leads to plasma cooling and lower efficiency.

To further understand sheath dynamics, laser-induced fluorescence is employed to provide a non-invasive, *in situ*, and spatially resolved technique for measuring xenon ion velocity. By scanning the laser wavelength over an electronic transition of singly ionized xenon and collecting the resulting fluorescence, one can determine the ion velocity from the Doppler shifted absorption. Knowing the velocity at multiple points in the sheath, it can be converted to a relative electric potential profile which can reveal a lot about the plasma-wall interaction and the severity of SEE.

The challenge of adequately measuring sheath potential profiles is optimizing the experiment to maximize the signal-to-noise ratio. A strong signal with low noise, enables high resolution measurements and increases the depth of measurement in the sheath, where the signal strength is lowest. Many improvements were made to reduce the background luminosity, increase the fluorescence intensity and collection efficiency, and optimize the signal

processing equipment. Doing so has allowed for a spatial resolution of 60 microns and a maximum depth of measurement of  $\sim 2$  mm depending on conditions. Sheaths surrounding common Hall thruster ceramics at various plasma conditions were measured in an attempt to determine the effect of SEE and a numerical analysis of the plasma-wall interactions was conducted to further understand the phenomena and compare against obtained data.

## ACKNOWLEDGMENTS

I want to thank everyone who supported me throughout my graduate program. This project presented many difficulties and I could not have done it without the help and guidance from others. I would like to thank my research advisor, Dr. Azer Yalin, for his willingness to provide help and support whenever I needed and for the incredible opportunity to work on this project. I also want to thank Dr. John Williams, who continued to help me through thick and thin even after many calls and office hour visits.

Many thanks to the incredible students of the Center for Laser Sensing and Diagnostics. Jordan Rath, Adam Friss and Brian Lee, thank you for your advice and countless discussions. Ciprian Dumitrache—I am very grateful for the endless help you provided, and I learned a lot from you. Jessica Tryner, Torben Grumstrup and Tim Vaughn, thank you for the technical support. It has been great working with all of you and I wish you all the best of luck in your future careers.

I want to thank Kapil Sawlani, John Foster and Alec Gallimore at the University of Michigan for designing and fabricating the plasma discharge. Samuel Langendorf also deserves thanks for the helpful discussion and patiently answering my questions.

And last but not least—I want to thank my family, especially my parents, for their endless support and love.

## TABLE OF CONTENTS

Abstract .....	ii
Acknowledgments.....	iv
List of Tables .....	vii
List of Figures .....	viii
1 Introduction .....	1
1.1 Hall Thrusters.....	1
1.2 Plasma-Wall Interactions.....	3
1.2.1 Classical Sheath Theory.....	3
1.2.2 Secondary Electron Emission .....	8
1.2.3 Space-Charge-Limited Sheath Regime.....	10
1.2.4 Other Sheath Regimes .....	13
1.2.5 SEE Effect on Hall Thrusters .....	14
1.3 Plasma Diagnostic Techniques .....	14
1.3.1 Plasma Bulk .....	15
1.3.2 Sheath.....	16
1.3.3 Related LIF Work.....	17
1.4 Objectives .....	18
2 Numerical Modeling.....	19
2.1 Introduction.....	19
2.2 Emissive Sheath Analysis.....	20
2.2.1 Discussion .....	24

3	Measurement Technique and Instrumentation . . . . .	27
3.1	Plasma Source . . . . .	27
3.1.1	Langmuir Probe . . . . .	31
3.2	LIF Scheme and Experimental Setup . . . . .	34
3.2.1	LIF Scheme . . . . .	34
3.2.2	LIF Saturation . . . . .	35
3.2.3	Sheath Potential Calculation . . . . .	36
3.2.4	Experimental Setup . . . . .	38
3.2.5	Experimental Limitations . . . . .	40
3.3	Data Processing Method . . . . .	42
3.4	Optimization Techniques . . . . .	46
3.4.1	Signal Improvement . . . . .	46
3.4.2	Noise Reduction . . . . .	48
3.4.3	Signal Processing Optimization . . . . .	49
4	Results and Discussion . . . . .	54
4.1	Demonstrative Sheath Measurement . . . . .	54
4.2	Repeatability Test . . . . .	56
4.3	Wall Material Effect . . . . .	58
5	Conclusion and Future Work . . . . .	63
5.1	Conclusion . . . . .	63
5.2	Future Work . . . . .	63
	References . . . . .	65

## LIST OF TABLES

1.1	Secondary electron yield power fit coefficients .....	11
4.1	Plasma conditions of repeatability test .....	56
4.2	Plasma conditions of wall material tests .....	58
4.3	Simulated sheath voltage with and without SEE yield .....	61

## LIST OF FIGURES

1.1	Picture and diagram of a Hall thruster .....	1
1.2	Eroded Hall thruster .....	2
1.3	Typical sheath potential profile .....	6
1.4	Plasma density representation in a sheath .....	7
1.5	Contribution of various types of electron emission .....	9
1.6	Secondary electron yield data from various materials .....	10
1.7	Secondary electron emission effect of sheaths .....	12
1.8	General types of sheath profiles .....	13
2.1	Numerical analysis results showing the effect of primary electron energy and density fraction on SEE yield and sheath voltage .....	23
2.2	Numerical analysis results of low primary energy effect on SEE yield .....	25
3.1	Diagram of the plasma source .....	28
3.2	Diagram and photo of the plasma bridge neutralizer .....	29
3.3	Plot of plasma density and Debye length versus discharge current .....	30
3.4	Ideal voltage-current curve from a Langmuir probe .....	31
3.5	Experimental Langmuir data with fit .....	33
3.6	Transition diagram of LIF .....	35
3.7	Doppler shifted LIF signal diagram .....	36
3.8	LIF plot of the dual peak .....	37
3.9	Schematic diagram of experimental setup .....	38
3.10	Plots of raw experimental data .....	43
3.11	Eatlon peak fit .....	44
3.12	LIF dual peak with fit .....	45

3.13	LIF signal improvement from larger collection lens .....	47
3.14	LIF signal improvement from beam expansion .....	48
3.15	Noise reduction from plasma bridge neutralizer .....	49
3.16	LIF signal improvement with increasing time constant .....	50
3.17	Comparison of averaging versus time constant .....	52
4.1	Demonstrative sheath profile .....	54
4.2	Sheath potential profiles of repeatability test .....	57
4.3	Sheath potential profiles from wall material tests.....	59

# 1 Introduction

This first chapter of this thesis will discuss the motivation behind the research in section 1.1, theory behind plasma-wall interactions in section 1.2, plasma diagnostic techniques and related work in section 1.3 and finally the objective of this work in section 1.4.

## 1.1 Hall Thrusters

Electric propulsion systems are gaining popularity in the aerospace field as a viable option for long term positioning and thrusting applications. In particular, Hall-effect thrusters (HETs, also called Hall thrusters) have shown promise as the primary propulsion engine for space probes during interplanetary journeys, as demonstrated by the successful SMART-1 Moon flyby solar-powered mission of the European Space Agency.<sup>1</sup> In addition, NASA's recently proposed Asteroid Redirect Mission has plans to use the Hall Effect Rocket with Magnetic Shielding (HERMeS, a 12.5 kW HET) on board the robotic spacecraft to transport

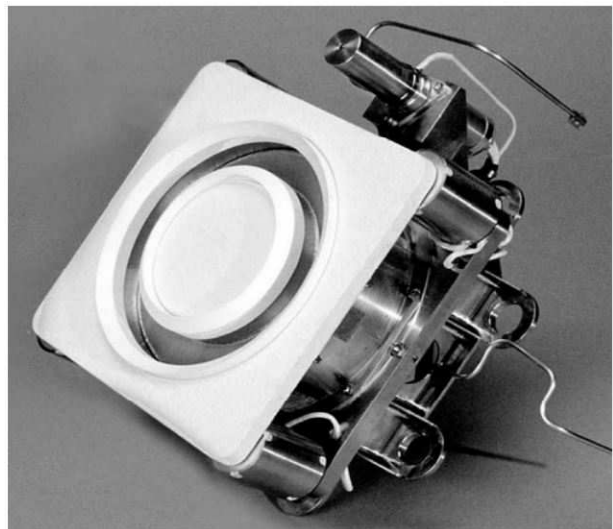
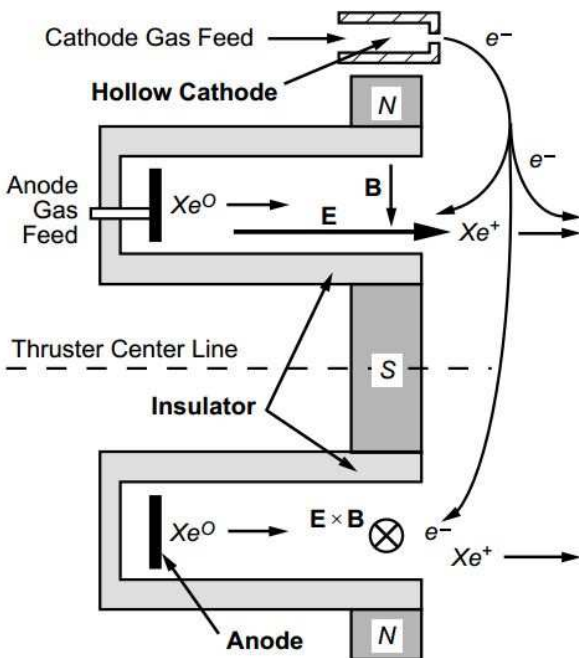


Figure 1.1: Left: Schematic illustration of HET showing direction of the magnetic and electric fields.<sup>2</sup> Right: Photograph of a BPT-4000 HET manufactured by Aerojet.

an asteroid into a stable lunar orbit. Hall-effect thrusters utilize a cross-field discharge described by the Hall effect to create the plasma and generate thrust by exhausting ions at a very high velocity.<sup>2</sup> A cross-sectional view of a HET is shown in Figure 1.1 and comprises of the anode, hollow cathode, and a cylindrical ceramic channel (typically boron nitride or borosilicate) surrounded by a magnetic circuit. The magnetic circuit and anode set up a radial magnetic field and axial electric field. A portion of the electrons generated by the hollow cathode are pulled into the channel by the positively charged anode and trapped by the  $\mathbf{E} \times \mathbf{B}$  drift to create the Hall current. The Hall current comprises the azimuthally circulating electrons within the channel that does the work of ionizing the stream of neutral propellant injected at the anode. Xenon is a commonly used propellant due to its low ionization energy per unit mass.<sup>3</sup> Newly created ions, which are unaffected by the magnetic field due to their larger Larmor radii, are then accelerated out by the strong axial electric field to propel the spacecraft.<sup>3</sup> The other electrons from the hollow cathode continue on with the exhausted plume to neutralize it, preventing a charged spacecraft and redeposition. As ions exit the channel, they occasionally impact the ceramic wall causing sputter erosion (see Figure 1.2). Sputter erosion is the process by which a energetic particle bombards a solid material and ejects atoms from it. If erosion is allowed to continue long enough, the

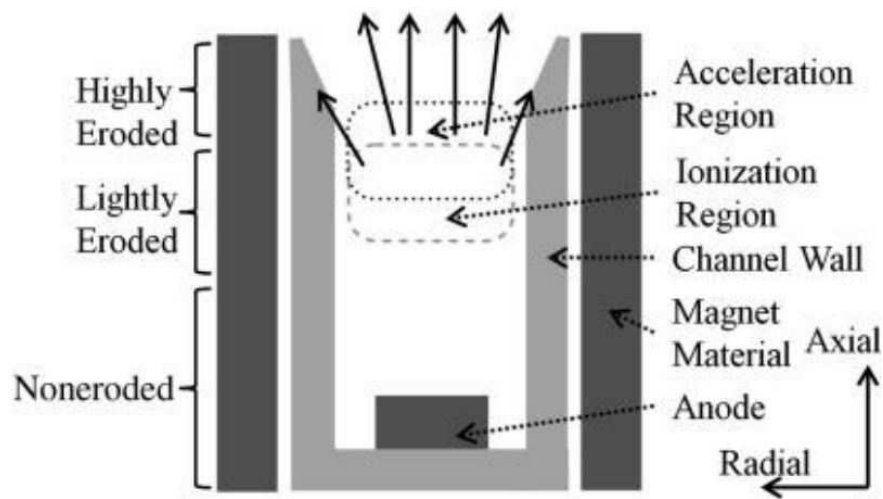


Figure 1.2: Erosion characteristics in HET discharge channel.<sup>4</sup>

ceramic wall can be completely eroded away, exposing the magnetic circuit. Further erosion damages the ferrous material which, alters the magnetic field, affecting HET performance and the ejected metal can redeposit onto the spacecraft, destroying electrical isolations.<sup>4</sup>

Recently, magnetically shielded thrusters have been developed that alter the magnetic field near the walls to reduce the ion-accelerating electric field parallel and perpendicular to the wall and the flux of ions to the wall.<sup>5</sup> These alterations very effectively reduce the sputter erosion rate. The first magnetically shielded Hall thruster propulsion system was jointly developed by Aerojet and Lockheed Martin Space Systems Company in the late 2000s. Grys et al.<sup>6</sup> showed no measurable insulator ring erosion from 5,600 hours to 10,400 hours indicating that this thruster had reached a 'zero' erosion configuration. The physics behind this magnetically shielded thruster was then described by JPL<sup>5</sup> who later tested a magnetically shielded version of the H6MS and found the power density increased by 50% while erosion reduced by orders of magnitude.<sup>7</sup> Although the development of magnetically shielded thrusters marks a large step forward in terms of life, very little in improvement to thruster efficiency was observed and furthering the understanding of wall effects is still critical to the development of higher efficiency Hall thruster technology. A more detailed discussion of how plasma-wall interactions affect HETs is in section 1.2.5.

## **1.2 Plasma-Wall Interactions**

### **1.2.1 Classical Sheath Theory**

A plasma is one of the four states of matter that is comprised of a quasineutral gas of charged and neutral particles which exhibits collective behavior.<sup>8</sup> It is a mix of an approximately equal number of free electrons and ions (over a large volume) that generates and reacts to electric and magnetic fields. A plasma can contain ions that are multiply ionized, but in this work, only singly ionized xenon atoms are studied. The free electrons are much less massive than the ions and more energetic, resulting in a much higher average speed. Due to high electron mobility, an electrically isolated surface (also referred to as a boundary or wall) in contact with a plasma will initially have a higher electron flux, which charges it

negatively. This negative charge then attracts the positively charged ions, which changes the wall potential until the net charge flux is zero. The wall potential at this condition is called the floating potential ( $\phi_f$ ). It is negative compared to the plasma potential ( $\phi_p$ ) to retard the electron current enough to match the ion current.

A fundamental characteristic of a plasma is its ability to shield out electric potentials that differ from the bulk plasma. This process, known as Debye shielding, gives rise to sheaths. A sheath is a boundary between the bulk plasma and any surface due to the electric potential difference. Plasmas are considered to have an infinite conductivity, which results in no electric fields present in the bulk plasma, therefore the electric field between the bulk plasma and the wall must exist in the sheath. Low energy electrons are repelled by the high electric field in the sheath and ions are accelerated, so therefore, the sheath is not considered a plasma due to the lack of quasineutrality. At steady state, the following equations describe current to the wall and the particle density in the sheath. The ion current flowing to the wall is given by

$$I_i = \frac{1}{2} e n_i A_{sh} \sqrt{\frac{k T_{ep}}{M}} \quad (1.1)$$

where  $n_i$  is the ion number density in the bulk plasma,  $A_{sh}$  is the ion collecting sheath area,  $e$  is the elementary charge,  $k$  is the Boltzmann constant,  $T_{ep}$  is the Maxwellian electron temperature in units of kelvin, and  $M$  is the ion mass. Equation 1.1 is more commonly known as the "Bohm current" where  $\exp(-1/2) = 0.607$  is approximated as  $1/2$ .

Ion density is given by

$$n_i(x) = n_0 \left( 1 - \frac{\phi(x)}{\phi_0} \right)^{-1/2} \quad (1.2)$$

where  $x$  is the location in sheath ( $x = 0$  at sheath edge),  $n_i(x)$  is the ion number density,  $n_0$  is the ion number density at the sheath edge (assuming quasineutrality,  $n_0 = n_i = n_{ep}$  in plasma bulk),  $\phi(x)$  is the local electric potential relative to the sheath edge (typically negative) and  $\phi_0$  is the electric potential at the sheath edge.<sup>2</sup>

The electron current flowing to the wall is the random electron flux times the Boltzmann factor, given by

$$I_e = \frac{1}{4} e n_{ep} A_{sh} \sqrt{\frac{8kT_{ep}}{\pi m_e}} \exp\left(-\frac{e\phi_s}{kT_{ep}}\right) \quad (1.3)$$

where  $n_{ep}$  is the plasma (Maxwellian) electron number density in the bulk plasma,  $m_e$  is the mass of an electron and  $\phi_s$  is the sheath voltage, which is the total potential drop across the sheath and is an unsigned number by convention.

Electron density is given by the Boltzmann relation

$$n_{ep}(x) = n_0 \exp\left(\frac{e\phi(x)}{kT_{ep}}\right), \quad (1.4)$$

where  $n_{ep}(x)$  is the plasma electron number density at location  $x$  within the sheath.

Equating the electron and Bohm current to solve for the sheath voltage yields

$$\phi_s = \frac{kT_{ep}}{e} \ln \left[ \sqrt{\frac{2M}{\pi m_e}} \right]. \quad (1.5)$$

This voltage is the amount that a floating surface will self-bias below the plasma, to maintain zero net current between itself and the plasma.

The characteristic distance of a sheath is called the Debye length where the total sheath thickness is dependent on plasma conditions and of the order of several Debye lengths. The Debye length is given by

$$\lambda_D = \left( \frac{\epsilon_0 kT_{ep}}{n_{ep} e^2} \right)^{1/2}, \quad (1.6)$$

where  $\epsilon_0$  is the permittivity of free space. The Debye length represents the maximum length scale over which a plasma can depart significantly from charge neutrality.<sup>8-10</sup> On length scales longer than the Debye length, a plasma responds collectively to a given charge, charge perturbation, or imposed electric field.<sup>9</sup>

This criterion for Debye shielding sheaths is only valid where the sheath voltage is small compared to electron temperature ( $e\phi_s \ll kT_{ep}$ ). If the sheath voltage is on the order of

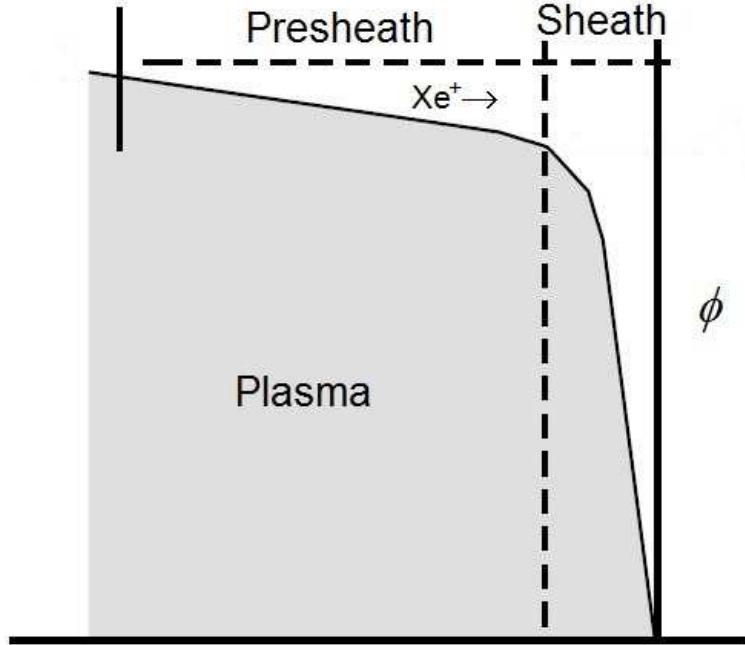


**Figure 1.3:** Typical potential profile of the classical plasma-wall interaction with presheath, adapted from Goebel.<sup>2</sup>

the electron temperature, then cold ions approaching the wall must fall through a potential (see Figure 1.3) in the plasma of at least  $kT_{ep}/(2e)$  before entering the sheath to produce a monotonically decreasing sheath potential profile.<sup>2,11,12</sup> This region where quasineutrality still exists over a Debye length, despite having a weak electric field to repel electrons, is referred to as the presheath. The scale of the presheath is set by either the ion mean free path, or the plasma radius, whichever is shorter.<sup>13</sup> The Bohm sheath criterion states that the ion's velocity at the sheath-presheath boundary must be greater than or equal to the ion acoustic velocity.<sup>12</sup> When this occurs, it forces the ion density to always be larger than the electron density through the sheath (see Figure 1.4), resulting in the physically realistic monotonically decreasing potential profile governed by Poisson's equation.<sup>2</sup> The Bohm velocity, defined as the ion acoustic velocity, is given by

$$u_B = \sqrt{\frac{kT_{ep}}{M}}. \quad (1.7)$$

Equation 1.2 can be rewritten to include the Bohm velocity, given as

$$n_i(x) = n_0 \left( 1 - \frac{2e\phi(x)}{Mu_B^2} \right)^{-1/2}. \quad (1.8)$$

If the potential drop across the sheath is large compared to the electron temperature ( $e\phi_s \gg kT_{ep}$ ), then the comparatively small potential drop in the presheath can be neglected and the assumptions are: ions enter the sheath at a zero velocity and the sheath is electron free.<sup>2,15,16</sup> This type of sheath is described by the Child-Langmuir model was originally derived by Child<sup>17</sup> in 1911 and then again, but independently, by Langmuir<sup>18</sup> in 1913. Using the Child-Langmuir model, ion current density is given by

$$J_i = \frac{4\epsilon_0}{9} \left( \frac{2e}{M} \right)^{1/2} \frac{\phi_s^{3/2}}{d^2}, \quad (1.9)$$

where  $J_i$  is in units of amperes per square meter and  $d$  is the sheath thickness. Equation 1.9 states that the space-charge-limited ion current that can pass through a sheath is proportional to the sheath voltage to the 3/2 power divided by the sheath thickness squared.

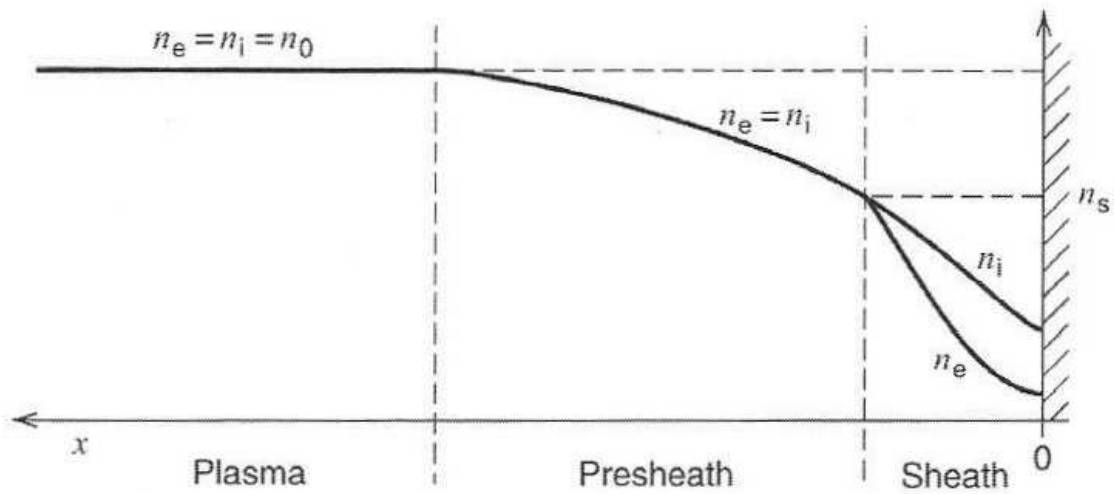


Figure 1.4: Density versus distance representation in the sheath and presheath, adapted from.<sup>14</sup>

The sheath thickness<sup>16</sup> is given by

$$d = \frac{2^{5/4} \lambda_D}{3} \left( \frac{e\phi_s}{kT_{ep}} \right)^{3/4}. \quad (1.10)$$

### 1.2.2 Secondary Electron Emission

Particles that make it through the sheath and impact the wall may cause the emission of an electron from the surface, which can further affect sheath characteristics. Although electron emission can also occur through thermionic emission from heating, and photoelectric emission from ultraviolet light,<sup>19</sup> secondary electron emission (SEE) is the only form of emission considered in this work. In addition, only electron-induced emission is considered in this work because ion-induced emission is not believed to play a significant role, since it is generally negligible for ion energies below 1 keV.<sup>20</sup> The secondary electron yield  $\gamma$ , is defined as

$$\gamma = \frac{\text{average number of emitted electrons}}{\text{incident electron}}. \quad (1.11)$$

Emitted electrons can be backscattered, rediffused, or emitted as true secondary electrons (see Figure 1.5)<sup>21,22</sup> and use of SEE yield  $\gamma$ , in this work will refer to the total emission of all three components. Backscattered electrons are incident electrons that have been elastically reflected by atoms at the surface of the wall material and therefore are re-emitted at the same incident energy.<sup>23</sup> Rediffused electrons are those that have undergone an inelastic collision with the surface atoms and are therefore re-emitted with an energy less than the incident energy. True secondary electrons originate from within the material and are ejected due to ionization or excitation collisions of surface atoms by electron impact.<sup>23</sup> Secondary electron emission is heavily dependent on impact energy and produces an electron that is typically much less energetic.<sup>22-24</sup> Free electrons originating from a plasma (as opposed to an electron gun) that impact the wall, do lose energy to overcome the sheath voltage which in turn affects the SEE yield.

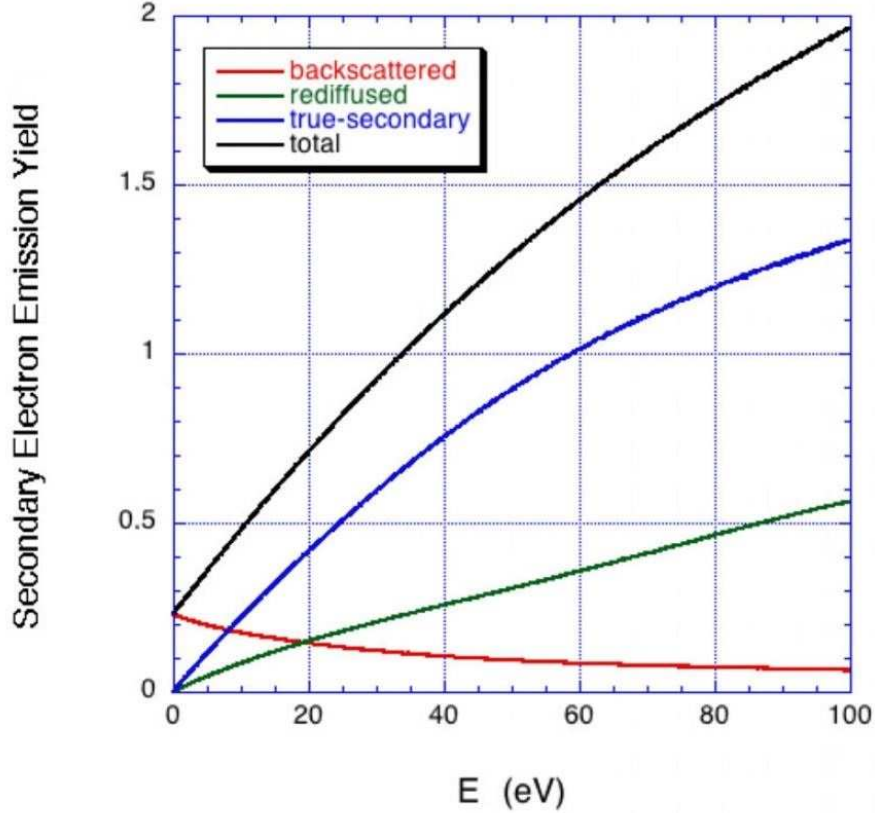


Figure 1.5: Total secondary electron emission yield  $\gamma$  (black) is the sum of backscattered (red), rediffused (green) and true secondary (blue) which are all a function of the monoenergetic impact electron energy  $E$ .<sup>3</sup>

Secondary electron yield data from common Hall thruster wall materials has been gathered and compiled by Goebel et al.<sup>2</sup> to develop a power fit relating electron bombardment energy to  $\gamma$  given by

$$\gamma = \Gamma(2 + b)aE^b \quad (1.12)$$

where  $\Gamma(x)$  is the gamma function, the coefficients  $a$  and  $b$  found in Table 1.1 are from fits to the data in Figure 1.6 and  $E$  is the electron impact energy in units of electron volts.

With an electron emitting wall the charge flux balance then becomes

$$\Gamma_i = \Gamma_e - \Gamma_{se} = \Gamma_e - \gamma\Gamma_e = \Gamma_e(1 - \gamma) \quad (1.13)$$

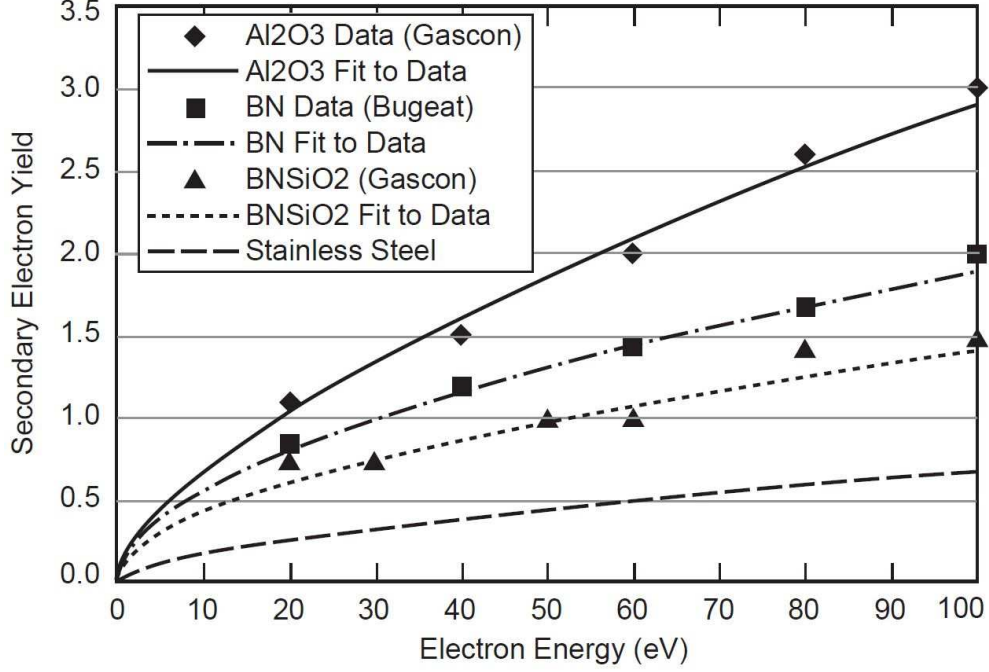


**Figure 1.6: Secondary electron yield for stainless steel and common wall materials used in Hall thrusters, measured with a monoenergetic electron beam.<sup>2</sup>**

where  $\Gamma_e$  and  $\Gamma_i$  are the electron and ion particle flux to the wall, respectively, and  $\Gamma_{se}$  is the secondary electron flux leaving the sheath. Equation 1.5 can be modified to include secondary electron yield, where the voltage of an emissive sheath is given by

$$\phi_s = \frac{kT_{ep}}{e} \ln \left[ (1 - \gamma) \sqrt{\frac{2M}{\pi m_e}} \right]. \quad (1.14)$$

### 1.2.3 Space-Charge-Limited Sheath Regime

As yield ( $\gamma$ ) increases with increasing electron impact energy, the sheath voltage decreases compared to the classic case of a plasma interacting with a non-emissive surface. A lower voltage ( $\phi_s$ ) allows more electrons to impact the wall to balance out the net electron current leaving the wall. The extremely high loss to the wall caused by the heavily reduced sheath voltage also imposes a virtual upper limit in the electron temperature, provided the electron velocity distribution function (EVDF) is Maxwellian.<sup>25</sup> If the yield approaches some critical value  $\gamma_{cr}$ , close to but less than unity, the electron influx increases rapidly as  $\Gamma_e = \Gamma_i / (1 - \gamma)$ ,

**Table 1.1: Fitting parameters for secondary electron yield from various materials.**

	a	b	$\Gamma(2 + b)$
Alumina ( $Al_2O_2$ )	0.145	0.650	1.49
Boron Nitride ( $BN$ )	0.150	0.549	1.38
Borosil ( $BN - SiO_2$ )	0.123	0.528	1.36
Stainless Steel	0.040	0.610	1.44

and the emission,  $\Gamma_{se} = \gamma\Gamma_i/(1-\gamma)$ , becomes intense enough that the negative charge formed by the secondaries creates a potential barrier near the surface.<sup>25,26</sup> This significant negative charge, that accumulates near the wall, creates an electric potential minimum in the sheath referred to as a virtual cathode, which returns a portion of the emitted electrons back to the wall.<sup>25</sup> An emissive sheath with these conditions (see Figure 1.7) is in a space-charge-limited (SCL) regime and is considered to be at the extrema of plasma-wall interaction.<sup>25,27-30</sup> In this regime, the net emission yield saturates to a critical value below unity, approximately given by

$$\gamma_{cr} = 1 - 8.3 \left( \frac{m_e}{M} \right)^{1/2} \quad (1.15)$$

so that Equation 1.13 can still be satisfied.<sup>2,26,29-31</sup> Hobbs and Wesson<sup>28</sup> found the solution to this important regime of plasma interaction based on an approximate analytic method for a marginally stable sheath when the electrostatic potential from the Poisson's equation is forced to be real at the sheath edge.<sup>29,30</sup> For infinitely massive ions, the Hobbs and Wesson theory<sup>28</sup> predicts the ion velocity at the sheath edge to be  $1.16u_B$ <sup>29</sup> and the sheath voltage to be

$$\phi_s \approx 1.02 \frac{kT_{ep}}{e}. \quad (1.16)$$

Equation 1.16 can be reasonably used to approximate a xenon plasma sheath for which  $\gamma_{cr} \approx 0.983$  from Equation 1.15.<sup>2</sup>

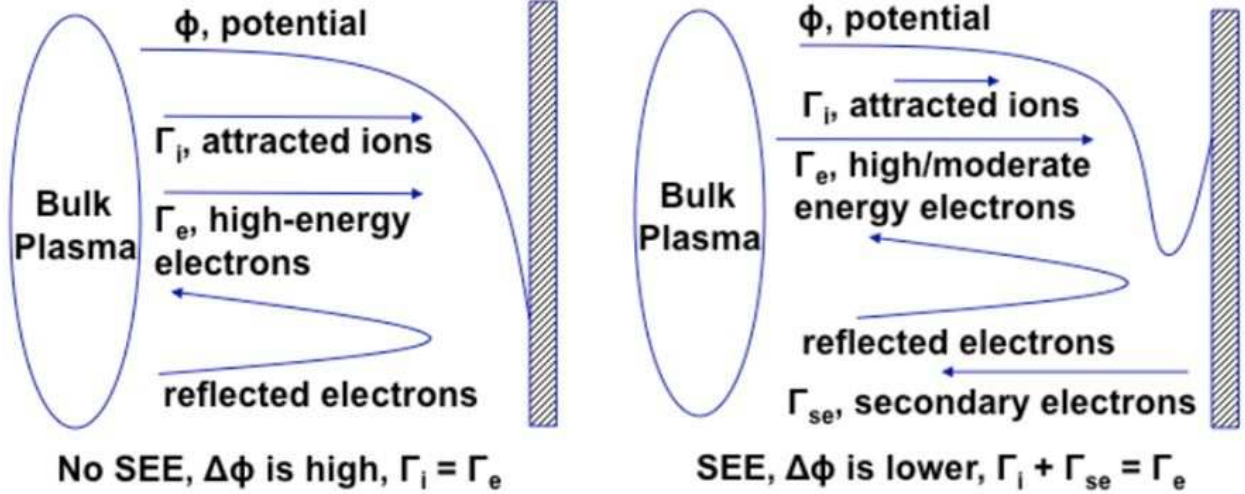


Figure 1.7: Sheath potential profiles with no emission (left); and with significant emission causing a virtual cathode (right).<sup>32</sup>

In the SCL regime, the sheath is no longer monolayered (or monotonic) as it is in the classical sheath, and is known as a double, or double layered sheath due to the counter flowing current.<sup>2,3</sup> A second electronegative layer of electrons exists near the wall causing the second derivative of the potential to change sign.<sup>22</sup> Assuming ions and secondary electrons opposingly enter the sheath with zero initial velocity, the SCL current density from an electron emitter through the sheath is given by

$$J_e = \sqrt{\frac{M}{m_e}} J_i, \quad (1.17)$$

and is known as the Langmuir condition,<sup>33</sup> which also describes the interaction of two plasmas at the separation boundary. To account for finite initial particle velocities, Andrews and Allen<sup>34</sup> developed a correction coefficient  $\beta$ , multiplied to the left hand side of Equation 1.17. The coefficient varies approximately with the electron to ion temperature ratio where  $\beta = 0.8$  at  $T_{ep}/T_i = 2$  and  $\beta = 0.2$  at  $T_{ep}/T_i = 20$ . For typical thruster plasmas where  $T_{ep}/T_i \approx 10$ ,  $\beta \approx 0.5$ .<sup>2</sup>

### 1.2.4 Other Sheath Regimes

Results of recent simulations<sup>25,26,35</sup> and kinetic analyses<sup>19,36</sup> of plasmas interacting with strongly emissive surfaces show that regimes beyond the space-charge-limited sheath exist. Equation 1.14 predicts that the sheath potential profile over a floating surface will flatten or reverse polarity (see Figure 1.8), as the secondary electron yield exceeds  $\gamma_{cr}$  and approaches unity.<sup>2</sup> An approximate value of the monoenergetic electron impact energy needed to reverse the sheath for various materials can be determined from Figure 1.6 where the power fit intersects a yield of one. Campanell et al.<sup>26</sup> simulated an inverted plasma sheath using electro-static direct implicit particle-in-cell (EDIPIIC) code showing a case where electrons travel unimpeded to the wall and ion flux is negligible.

A simulation study done by Sydorenko et al.<sup>25</sup> showed that in a plasma with a Maxwellian electron temperature many times greater than the critical temperature it is possible for the sheath to perform relaxation oscillations, thus never reaching a steady state. As the sheath voltage decreases from increasing SEE, the sheath enters the SCL regime, and once a wall encounters an intense flux of cold electrons from the opposite wall, the SCL regime quenches.

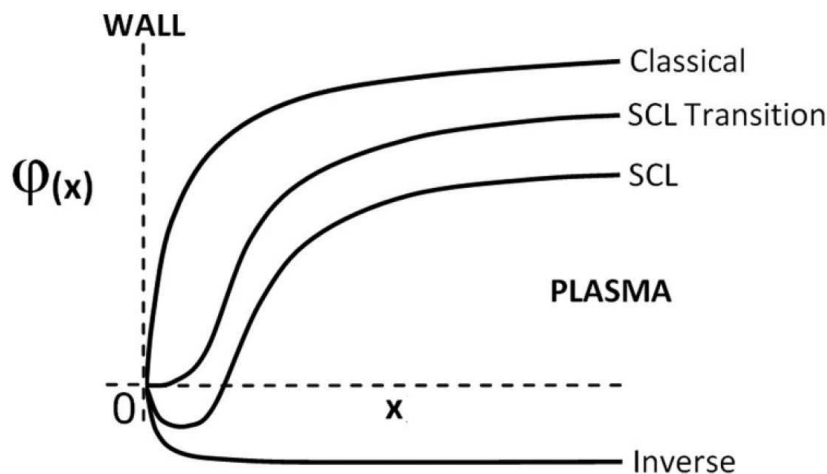


**Figure 1.8:** Graphical representation of sheath potential profiles in the classical (monotonic,  $\phi_f < \phi_p$ ), SCL (nonmonotonic  $\phi_f < \phi_p$ ) and inverse (monotonic,  $\phi_f > \phi_p$ ) sheath regimes where potential has been normalized by wall floating potential ( $\phi_f$ ).<sup>36</sup>

The trapped high density secondaries in the plasma bulk are then heated from collisions, and start the process all over again.

### 1.2.5 SEE Effect on Hall Thrusters

As described in the previous sections, SEE affects the sheath characteristics and with increasing SEE it increases an electron's probability of reaching the wall. In other words, an emissive surface reduces the sheath voltage and thus increases losses to the wall. The most significant source of power loss in dielectric-wall Hall thrusters (as opposed to the TAL thruster with metal channel walls) is due to electron and ion currents flowing along the radial magnetic field through the sheath to the channel walls.<sup>2</sup> With a reduced sheath voltage, the bombarding ion energy is lessened and so too the sputter erosion rate, but at the expense of higher losses to the wall.<sup>2</sup> Dielectric-wall HETs therefore trade efficiency for longer lifetime.

Studies by<sup>37-39</sup> of HET channel plasma indicate that the electron velocity distribution function is non-Maxwellian, anisotropic and depleted of high-energy electrons due to rapid loss to the wall. This results in plasma cooling because high energy electrons are replaced with lower energy secondaries.<sup>20,40</sup> A more comprehensive review on plasma-wall interaction affecting Hall thruster performance can be found in Refs.<sup>41-45</sup>

## 1.3 Plasma Diagnostic Techniques

Generally, there are two types of diagnostic approaches to study a system, invasive and non-invasive. Examples of invasive techniques include measuring air pressure with a pitot tube, measuring water temperature with a mercury thermometer, and studying a plasma with a Langmuir probe. The perturbation to the system of interest may be negligible depending on the situation, but not always. Non-invasive approaches include studying far off galaxies by collecting and analyzing the photons given off, and measuring ion velocity using laser-induced fluorescence. This section will discuss common invasive and non-invasive plasma diagnostic techniques related to this work.

### 1.3.1 Plasma Bulk

An important aspect of the work presented in this thesis is understanding and measuring the various bulk plasma parameters. A Langmuir probe is a popular device to measure plasma parameters including electron temperature, electron density and plasma potential, allowing calculation of other important parameters such as Debye length and Bohm velocity. Discovered by Irving Langmuir, and first discussed by Mott-Smith and Langmuir in 1926,<sup>46</sup> the Langmuir probe is simply a piece of metal of known dimensions (typically a wire, disk or sphere) inserted into a plasma. A single electrical connection is made to the probe to apply a potential bias above and below the floating and plasma potentials. Over a wide range of conditions, the current-voltage (I-V) curve can be analyzed to obtain the plasma parameters that are, in principle, present in the absence of the probe.<sup>47</sup> Although Langmuir probes are an invasive diagnostic technique, if the maximum current drawn by the probe is much much less than anode current of the plasma source, the perturbation is negligible. A more in-depth discussion of how a Langmuir probe works and is used in this work is given in Section 3.1.1.

Emissive probes provide a sensitive, relatively non-invasive, diagnostic of plasma potential with a resolution of about 0.1 V and 0.1 cm spatially.<sup>48</sup> It is a probe consisting of thin metal wire, typically tungsten, 25 microns in diameter and 0.5 cm long, inserted into at plasma. This probe fundamentally differs from a Langmuir probe because the probe is part of a completed circuit, meaning there are two electrical leads connected to this probe to run current through it. The thermionically emissive wire emits electrons when it is biased negative relative to the plasma potential and emission is suppressed when the probe is biased positive relative to plasma potential. Plasma potential is then determined by sweeping the biased potential of the wire to record a current-voltage curve and where the inflection point occurs in the data is the plasma potential. A common use of emissive probes is to measure the spatial potential variation of a Hall thruster plume.

A Wein Filter, also known as an  $\mathbf{E} \times \mathbf{B}$  probe, is an ion velocity measurement tool. It is a device that allows a small unidirectional stream of ions to enter, and as they pass through

the internal tunable  $\mathbf{E} \times \mathbf{B}$  field, their trajectory can be altered based on velocity. Ions with the desired velocity travel undeflected to the end, and strike a collector plate which produces a measurable current. Since the velocity of the ions is dependent on their mass and thus charge-state, an  $\mathbf{E} \times \mathbf{B}$  probe can be used to determine the ion velocity distribution across multiple ion species.<sup>49</sup>

### 1.3.2 Sheath

Understanding sheaths is perhaps one of the oldest problems in plasma physics<sup>17,18</sup> and measuring sheath potential profiles are difficult. Electric fields in sheaths in many laboratory plasmas are on the order or smaller than 100 V/cm or less and can be thinner than 1 mm.<sup>48</sup> Langmuir probes are easily capable of measuring bulk plasma properties, but operate by generating their own sheath, and therefore cannot accurately measure parameters in the sheath naturally surrounding walls. Emissive probes have been used to measure sheath potential profiles,<sup>48,50,51</sup> but this technique is limited to thick sheaths ( $\gtrsim 1$  cm) due to the poor resolution. However, using laser-induced fluorescence (LIF) as a sheath diagnostic is non-invasive, *in situ*, and spatially resolved in three dimensions. It is perhaps the most popular technique dating back to the 1980s to study rf plasma sheaths,<sup>52,53</sup> and DC discharge sheaths in the early 1990s.<sup>54</sup> LIF uses a laser to excite a specific transition of an ion, and the photon emitted from the resulting spontaneous decay is collected and studied. If the laser is capable of scanning across the absorption frequency, one dimensional velocity information can be calculated from the Doppler shifted absorption. From there, it is a matter of collecting the fluorescence at different locations to obtain velocity versus distance data, which can be easily converted to relative potential versus distance.

Although LIF is non-invasive and has higher spatial resolution than physical probes, it can only measure potential differences, which is limited by a particular state of an ion, and can only measure where the ion density is relatively high. Because LIF inherently measures velocity, this data can only be used to determine a change in electric potential from the energy conservation law, whereas emissive probes can measure the absolute potential. Also, it is

limited by a specific state of the ion, for example, only singly ionized xenon in a metastable state can be exploited for this LIF scheme presented. Finally, detecting this extremely weak fluorescence signal in a high noise environment requires a relatively high density of ions present. A low density plasma deep within a sheath may not produce enough fluorescence to exceed the noise. On the other hand, emissive probes do not have this issue and have been used to determine the plasma potential in systems with number densities ranging from 'vacuum' to  $10^{19} \text{ m}^{-3}$ .<sup>48</sup> A fuller description of LIF and the experiment used in this work is given in Chapter 3.

### 1.3.3 Related LIF Work

As previously stated, the use of LIF to study plasma sheaths has been around since the 1980s. Since then, LIF has been used as a benchmark by Lam and Hershkovitz<sup>55</sup> to confirm the validity of other plasma diagnostic techniques. Furthermore, extensive research into ion velocity in single and multi-species plasma sheaths has been conducted by University of Wisconsin-Madison, University of San Diego and others.<sup>10,16,56-61</sup>

Researchers Goeckner et al.<sup>54</sup> studied plasma presheaths near a polished electrode to reflect the beam in order to provide a pseudo-absolute calibration of the LIF measurement (the relative frequency calibration is still necessary, but the absolute wavelength of the Doppler shifted absorption is unknown but not needed). In this method, the counter propagating beams produce two Doppler shifted LIF signal peaks where the frequency separation is directly related to twice the ion velocity, and conveniently provides a self-calibrated measurement without additional equipment. This measurement technique is identical to the one used in this work, further discussed in section 3.2.

Another method of frequency calibration of LIF sheath studies is by use of an external reference cell. Cells containing an absorbing media at a known frequency near the LIF transition (and within the laser scan range) are commonly used to provide the absolute frequency calibration of the laser light. The use of an iodine cell has been demonstrated<sup>62-64</sup> for studies with argon and xenon at the 611.6616 and 605.2781 nm transitions, respectively.

Another commonly used reference cell is a laser galvatron which produces a stable plasma. For example, when 834.974 nm light is shined through the Hamamatsu L2783-42 XeNe-Mo laser galvatron, neutral xenon absorbs the light and increases the plasma conductivity by a measurable amount via the optogalvanic effect. This cell has been used due to its proximity to the transition at 834.953 nm for xenon ions.<sup>65,66</sup> This galvatron was used early in this work, but due to reliability issues resulting from prolonged use, it was replaced by the self-calibrating method. For unique situations where a reference cell cannot be used, a high-finesse wavemeter can provide the relative and absolute laser frequency calibration.

#### 1.4 Objectives

Jordan Rath, a former masters student at the Center for Laser Sensing and Diagnostics at CSU, started preliminary work on this project before he graduated in late 2013. He laid some important ground work, but the experiment needed improvement to provide the capability of measuring plasma sheaths. Nearly every experimental variable, instrument, and device was rethought and redesigned in the present work, which ultimately improved the signal-to-noise ratio by a factor of  $\sim 200$ . This allowed measurements at low plasma density where thick sheaths exist, enabling high spatial resolution.

The objectives of this work are:

- Redesign and continuously improve the original experiment to enable high resolution sheath measurements.
- Using LIF, measure sheath potential profiles surrounding common Hall thruster ceramics at various plasma conditions to determine the effect of SEE.
- Conduct a numerical analysis of the plasma-wall interactions generated by the experiment to further understand the phenomena and compare against obtained data.

## 2 Numerical Modeling

### 2.1 Introduction

Simple models of the plasma wall interaction treat surfaces only as a sink for charged particles and the resulting assumption of equal incident electron and ion fluxes in equilibrium determines sheath properties.<sup>35</sup> Hobbs and Wesson<sup>28</sup> expanded on the work done by Child<sup>17</sup> and Langmuir<sup>18</sup> to develop a fluid theory including an emissive influence on the plasma-wall interaction. However, the non-Maxwellian electron distribution function (EDF) often found in laboratory plasmas and Hall-effect thrusters<sup>22,25,37,67</sup> cannot be directly treated by the Hobbs and Wesson theory.

In general there are two ways to describe a plasma, by use of a fluid model, or kinetic model. Fluid models describe the plasma as smoothed quantities by applying solutions of Boltzmann and Poisson's equations and assume particles follow a Maxwellian velocity distribution.<sup>68</sup> Whereas kinetic models describe plasmas as the effects of motion of charged particles, and therefore there is no need to assume any particular velocity distribution.<sup>69</sup> By removing some of the assumptions made in a fluid model, a kinetic model can be more accurate in describing a sheath.<sup>70</sup>

In recent years, many researchers have modeled plasma-wall interaction using both fluid and kinetic models. Cenian et al.<sup>68</sup> studied various types of plasma-wall interaction found in DC discharges with particle-in-cell Monte Carlo (a form of kinetic modeling) and fluid models. Sheehan et al.<sup>70,71</sup> used a kinetic model to study the effect of emitted electron temperature on the sheath potential and compared it to other methods. In addition many have used kinetic models to study the effect of secondary electron emission on Hall thruster performance and the plasma EDF .<sup>38,67,72</sup>

## 2.2 Emissive Sheath Analysis

The following is a kinetic analysis that combines the use of sheath boundary condition equations, electron distribution functions, and secondary electron yield data to further describe and understand the sheaths studied in this work. This kinetic model is an adaptation from Langendorf<sup>31,73</sup> and Sheehan.<sup>71</sup>

This analysis assumes two distinct groups of electrons contribute to SEE: a Maxwellian distribution of plasma electrons and a monoenergetic isotropic group of primary electrons. The density and energy of the plasma electrons is held constant, where as the primary electron density and energy is not. Primary electrons are a consequence of using a hot filament to produce energetic electrons for ionization of xenon (discussed further in Chapter 3). These electrons have maintained a high energy ( $E_{pri}$ ) but have lost directionality due to multiple bounces off the strong magnetic field gradients at the walls formed by the permanent magnets of the plasma source used in this work. Secondary electrons affect the boundary conditions and are involved in the analysis, but do not contribute to additional SEE due to a velocity vector pointing away from the wall. The sheath is assumed to be at steady state, one-dimensional, unmagnetized, collisionless (therefore source and sink free) and without thermionic emission from the wall. A secondary electron temperature is also assumed to be one-tenth of the plasma electron temperature ( $\theta = T_{ep}/T_{ee} = 10$ ).

The following equations describe the electron velocity distribution functions as piecewise equations describing the population with sufficient energy to reach the wall.

$$f_{ep}(u, \Phi) = \begin{cases} 0 & u \leq u_s \\ \sqrt{\frac{m_e}{2\pi T_{ep}}} \exp\left(-\frac{m_e u^2}{2T_{ep}} - \Phi\right) & u > u_s \end{cases} \quad (2.1)$$

$$f_{pri}(u, \Phi) = \begin{cases} 0 & u \leq u_s \\ \frac{1}{u_s(\Phi) + u_{pri}(\Phi)} & u_s < u < u_{pri} \\ 0 & u \geq u_{pri} \end{cases} \quad (2.2)$$

where

$$u_s(\Phi) = \sqrt{\frac{2T_{ep}}{m_e}(\Phi_s - \Phi)}, \quad (2.3)$$

$$u_{pri}(\Phi) = \sqrt{\frac{2T_{ep}}{m_e}(\epsilon_{pri} - \Phi)}, \quad (2.4)$$

$$\Phi = \frac{\phi}{T_{ep}}, \quad \Phi_s = \frac{\phi_s}{T_{ep}}, \quad \epsilon_{pri} = \frac{E_{pri}}{T_{ep}}. \quad (2.5)$$

Where  $f_{ep}(u, \Phi)$  and  $f_{pri}(u, \Phi)$  are the plasma (Maxwellian) and primary electron velocity distribution functions dependent on velocity ( $u$ ) and normalized local electric potential ( $\Phi$ ) and piecewise according to velocity required to penetrate the sheath and impact the wall  $u_s$ , and the monoenergetic isotropic primary electron velocity  $u_{pri}$ . These functions are applicable over any  $\Phi$  in the sheath that produce a real result, but this analysis only considers the boundary conditions. Although the wall floating potential is normally below the plasma potential, the normalized sheath voltage  $\Phi_s$  is positive by convention.

The boundary condition equations impose the following constraints: quasineutrality at sheath edge, balanced charge flux to and from the wall, SEE yield relation and the marginalized Bohm criterion. The marginalized Bohm criterion assumes ions enter the sheath at exactly the Bohm velocity (Equation 1.7) as opposed to greater than or equal to that velocity. These constraints are given by

$$0 = 1 - N_{ep0} - N_{ee0} - \left( \frac{\alpha}{1 - \alpha} \right) N_{ep0}, \quad (2.6)$$

$$0 = 1 - \frac{1}{\sqrt{\pi}} \frac{\exp(-\Phi_s) \sqrt{\mu/\epsilon_i}}{2 - \operatorname{erfc}(\sqrt{\Phi_s})} (N_{ep0}) + \frac{1}{\sqrt{\pi}\theta} \frac{\exp(-\Phi_s\theta) \sqrt{\mu/\epsilon_i}}{\operatorname{erfc}(\sqrt{\Phi_s}\theta)} (N_{ee0}) - \frac{1}{2} \left( \frac{\alpha}{1 - \alpha} \right) \left( \frac{\epsilon_{pri} - \Phi_s}{\sqrt{\epsilon_{pri}} + \sqrt{\Phi_s}} \right) (N_{ep0}), \quad (2.7)$$

$$0 = 0 - \frac{\gamma}{\sqrt{\pi}} \frac{\exp(-\Phi_s) \sqrt{\mu/\epsilon_i}}{2 - \operatorname{erfc}(\sqrt{\Phi_s})} (N_{ep0}) + \frac{1}{\sqrt{\pi}\theta} \frac{\exp(-\Phi_s\theta) \sqrt{\mu/\epsilon_i}}{\operatorname{erfc}(\sqrt{\Phi_s}\theta)} (N_{ee0}) - \frac{\gamma}{2} \left( \frac{\alpha}{1 - \alpha} \right) \left( \frac{\epsilon_{pri} - \Phi_s}{\sqrt{\epsilon_{pri}} + \sqrt{\Phi_s}} \right) (N_{ep0}), \quad (2.8)$$

$$0 = -\frac{1}{2\epsilon_i} - \left( \frac{1}{\sqrt{\pi}} \frac{\exp(-\Phi_s)}{\sqrt{\Phi_s}(\operatorname{erfc}(\sqrt{\Phi_s}) - 2)} - 1 \right) (N_{ep0}) - \left( \frac{\theta}{\sqrt{\pi}} \frac{\exp(-\Phi_s\theta)}{\sqrt{\Phi_s}\theta \operatorname{erfc}(\sqrt{\Phi_s}\theta)} - \theta \right) (N_{ep0}) + \frac{1}{2} \left( \frac{\alpha}{1 - \alpha} \right) \left( \frac{1}{\sqrt{\epsilon_{pri}\Phi_s}} \right) (N_{ep0}), \quad (2.9)$$

where

$$N_{ep0} = \frac{n_{ep0}}{n_0}, \quad N_{ee0} = \frac{n_{ee0}}{n_0}, \quad \theta = \frac{T_{ep}}{T_{ee}}, \quad \epsilon_i = \frac{E_i}{T_{ep}}, \quad \alpha = \frac{n_{pri0}}{(n_{pri0} + n_{ep0})}, \quad \mu = \frac{M}{m_e}. \quad (2.10)$$

Plasma and emitted electron densities at the sheath edge (denoted by zero in subscript), nondimensionalized by the ion density at the sheath edge are  $N_{ep0}$  and  $N_{ee0}$ , respectively. Ions at the sheath edge of density  $n_0$ , enter the sheath with energy  $E_i$  of normalized energy  $\epsilon_i$ . Density fraction of primary electrons with respect to plasma electrons at the sheath edge is given by  $\alpha$  and singly ionized xenon of mass  $M$ , is expressed in the mass ratio  $\mu$ .

The boundary condition Equations 2.6-2.9 are smooth, nonlinear, solved numerically and contain the four unknowns:  $\Phi_s$ ,  $\epsilon_i$ ,  $N_{ep0}$  and  $N_{ee0}$ . Where each term from left to right represents the ions, plasma electrons, secondary emitted electrons and primary electrons, respectively. An initial guess for SEE yield  $\gamma$  was used to solve for unknowns, then based

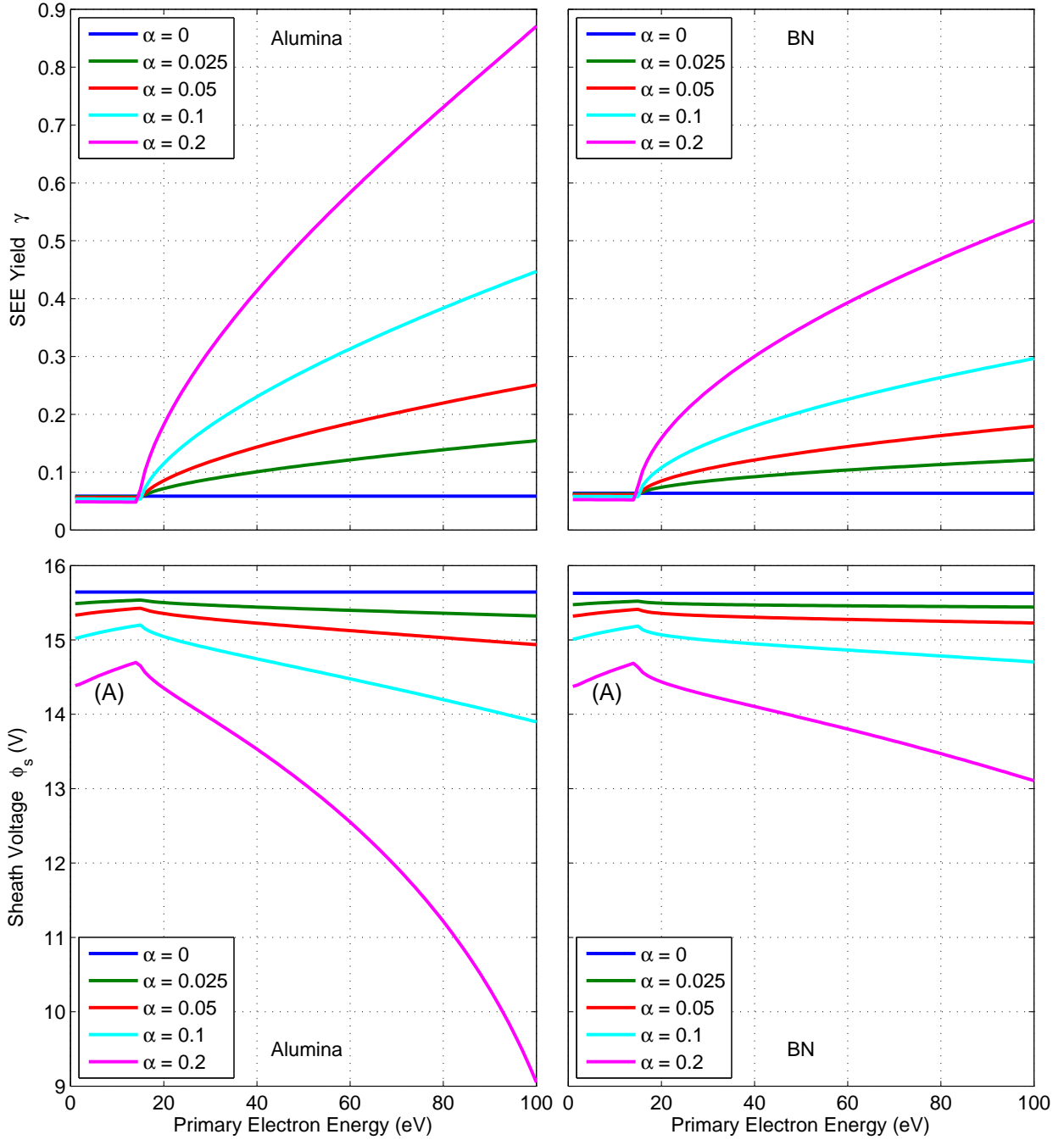


Figure 2.1: Effect of primary electron density fraction  $\alpha$  and energy on SEE yield (top) and sheath voltage (bottom) for alumina (left) and boron nitride (right). Plasma electron temperature  $T_{ep} = 3$  eV, density  $n_{ep} = 2.5 \times 10^{16} m^{-3}$ , and temperature ratio of plasma electrons to emitted electrons of  $\theta = 10$  are held constant. Data near region (A) described in text.

on the outcome of sheath voltage  $\Phi_s$ ,  $\gamma$  was resolved for and this process was repeated until values of  $\Phi_s$  and  $\gamma$  were converged upon. By stepping through a range and  $\alpha$  and  $E_i$ , a corresponding yield and sheath voltage was obtained for both alumina and boron nitride using the yield fit Equation 1.12 derived by Goebel et al.<sup>2</sup>

### 2.2.1 Discussion

Figure 2.1 shows how gamma  $\gamma$  and sheath voltage  $\phi_s$  are affected by varying isotropic primary electron energy  $E_{pri}$  and density fraction  $\alpha$  in the bulk plasma. Plasma electron temperature and density were fixed at  $T_{ep} = 3$  eV, and  $n_{ep} = 2.5 \times 10^{16} m^{-3}$ , respectively, which is a combination commonly measured by the Langmuir probe in this work. Comparing these results to Figure 1.6 shows the obvious affect a sheath has on the secondary electron emission yield. The retarding effect the sheath profile has on the incident electron energy affects the SEE yield, which in turn affects the sheath voltage.

In addition, comparing the theoretical sheath voltage to a measured sheath voltage by a Langmuir probe shows good agreement. Conditions determined by a Langmuir probe are  $n_{ep} = 2.4 \times 10^{16} m^{-3}$ ,  $\alpha = 0.061$ ,  $T_{ep} = 3.1$  eV,  $E_{pri} = 16$  eV,  $\phi_p = 33$  V and  $\phi_f = 16$  V, where the sheath voltage is,  $\phi_s = \phi_p - \phi_f = 17$  V. Assuming the Langmuir probe is stainless steel, the SEE yield power fit from Equation 1.12 can be used to determine the sheath voltage and SEE yield of an electrically floating Langmuir probe. Doing so results in  $\phi_s = 16.0$  V and  $\gamma = 0.016$ . Agreement between measured and calculated sheath voltage is excellent, and possible reasons for the small difference of  $\sim 1$  V between measured and calculated sheath voltage are incorrect material assumption and inaccurate estimation of SEE yield at low electron impact energy.

Alumina in general has a higher SEE yield and consequently a lower sheath voltage for a given primary electron energy (above  $\sim 15$  eV) and density fraction than BN. However, the data used to obtain the fit equation used to calculate  $\gamma$  as a function of monoenergetic temperature (Equation 1.12) may not be accurate below 20 eV, as this was the lowest energy data point used for the fit equation. Researchers Dunaevsky et al.<sup>74</sup> collected data

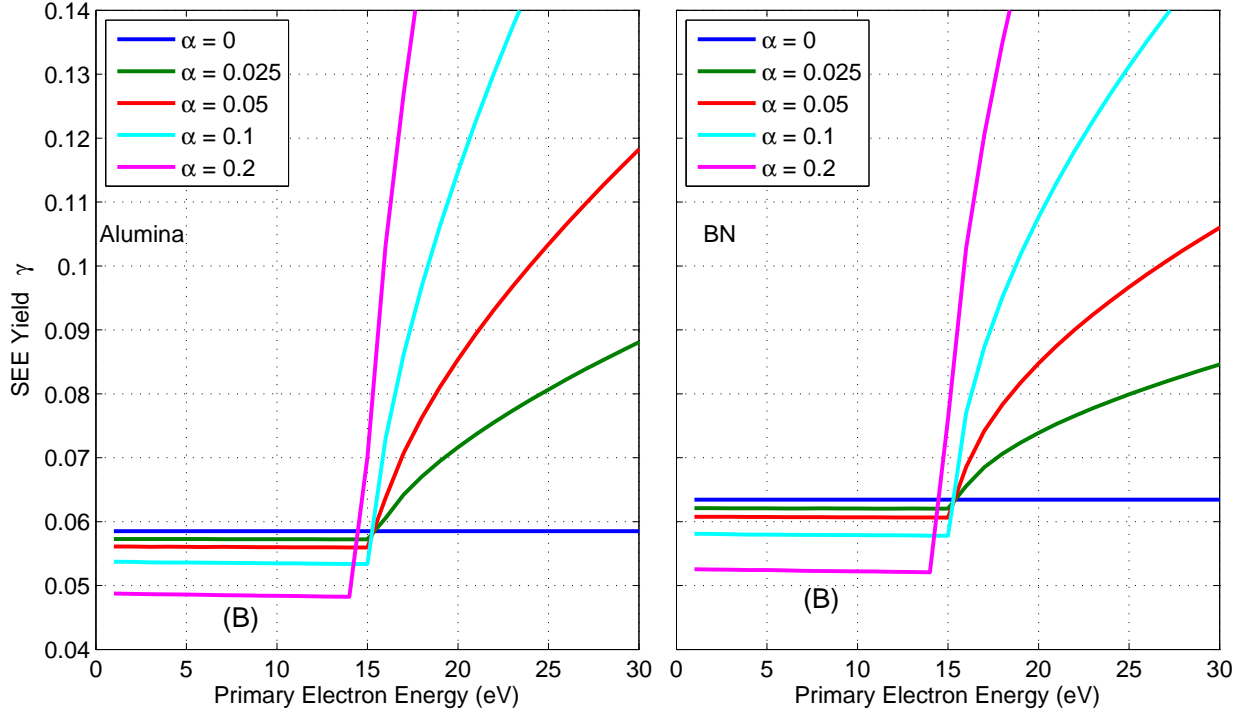


**Figure 2.2:** Zoomed in view of top row plots in Figure 2.1 showing the effect of primary electron density fraction  $\alpha$  at low energies on gamma for alumina (left) and boron nitride (right). Data near region (B) described in text.

that suggests the power fit used to estimate BN yield at low incident energies is inaccurate. As shown in Figure 2.2, boron nitride has a slightly higher yield for energies below 15 eV, which may be a consequence of an inaccurate yield estimation at low energies. However, at low primary electron energy, the density fraction is a far more important factor determining sheath characteristics than yield.

The following will explain regions of the analysis indicated by the letters near certain areas of the data in Figures 2.1 and 2.2.

(A) At low primary electron energy, the sheath voltage slowly increases with increasing primary energy, at a constant, non-zero primary density fraction ( $\alpha$ ). As primary electrons are more and more capable of penetrating deeper into the sheath with increasing energy, the local potential near the sheath-presheath boundary increases which decreases the sheath area and thus decreases the ion current (see Equation 1.1). The sheath responds by increasing the voltage to

prevent more electrons from reaching the wall to balance the charge flux. As primary energy exceeds the energy required to overcome the sheath at this particular plasma condition, secondary electron emission rapidly begins to increase (seen more clearly in Figure 2.2) particularly at high values of  $\alpha$ . To account for the more emissive wall, the sheath voltage drops to allow more electrons to reach the wall to maintain the balance of charge flux to the wall.

An increasing value of  $\alpha$  at a constant primary energy  $\leq 14$  eV, causes the total electron density to increase along with the ion density  $n_0$ . This reduces the relative amount of Maxwellian electrons in the high energy tail responsible for charge flux balance to the wall because  $n_{ep}$  is constant. In response, the sheath voltage decreases to allow a higher electron flux to match the increased ion flux.

(B) Another interesting aspect of this numerical analysis is the trend of the yield with varying primary electron density fraction. Secondary electron yield decreases with increasing  $\alpha$  (at a constant primary energy) because while  $T_{ep}$  and  $n_{ep}$  are constant, the incident electron energy distribution function changes with decreasing sheath voltage. At a lower sheath voltage the required energy to impact the wall decreases, which due to the Maxwellian distribution, allows a higher population fraction of low energy electrons to impact the wall. This increases the impact rate of the same low energy electrons and shifts the average impact energy to a lower energy and consequently lowers SEE yield due to its strong dependence on incident energy.

### 3 Measurement Technique and Instrumentation

Laser-induced fluorescence (LIF) was first developed by Richard Zare, in 1968 to test his idea of exciting molecules to produce fluorescence, an idea that was doubted by his former Harvard professor. Zare, at UC Boulder's JILA, built a He-Ne laser to study the potassium dimer molecule ( $K_2$ ), and discovered previously unknown vibrational-rotational levels using LIF.<sup>75</sup> While LIF can be used for many purposes such as measuring thruster plume velocity and temperature,<sup>76-78</sup> utilizing the Stark effect to measure time and space resolved electric fields in an rf plasma,<sup>79</sup> and sequencing the human genome using capillary electrophoresis separation via LIF;<sup>75</sup> it has increasingly become the favored diagnostic technique for plasma sheaths.

In this work, LIF is used to measure the one-dimensional xenon ion velocity orthogonal to a ceramic wall, throughout the plasma sheath. To accomplish this, a vacuum chamber, plasma source, diode laser, various optics, detectors, and electronic equipment is needed. This chapter presents how and what is used to measure the xenon ion velocity. Section 3.1 discusses the plasma source and Langmuir probe, section 3.2 describes the LIF scheme and the optics portion of the experiment, section 3.3 discusses data analysis, and section 3.4 the experimental improvements.

#### 3.1 Plasma Source

The plasma source used in this study is a multi-dipole DC discharge that was originally designed and fabricated by Professor John Foster's research group at the University of Michigan to provide a suitable test bed for optical sheath measurements. The source was designed to create low-density, unmagnetized plasmas with relatively thick, and collisionless sheaths near surfaces. It was operated in a relatively small table-top vacuum chamber capable of reaching a base pressure of  $1.1 \mu\text{Torr}$  and an operating pressure of  $200 \mu\text{Torr}$  at 1 sccm of xenon gas, as measured with an ion gauge. A rotary vane roughing pump (Trivac D30A) was used in conjunction with a turbo pump (Turbovac 150) to maintain low pressure and a

mass-flow controller (Celerity Unit 7360) to supply the xenon fed directly into the plasma source.

There are four main components to the plasma source: discharge, grid, plasma bridge neutralizer (PBN) and ceramic mount (see Figure 3.1). Xenon gas is fed into the PBN at the rear of the source which houses the hot tungsten filament to provide electrons for subsequent acceleration and ionization of neutrals (see Figure 3.2). The discharge is a cylindrically shaped container (roughly 20 cm in diameter and 15 cm deep) designed to contain the plasma and confine the electrons with a magnetic field generated by 4 internal rings of permanent magnets. The region in the center of the source where the measurements are made is nearly field-free. At the end of the discharge is the grid, it is a metal plate with hundreds of small ( $\sim 1/8$  inch) holes in a repeating hexagonal pattern that is held at a negative voltage to repel

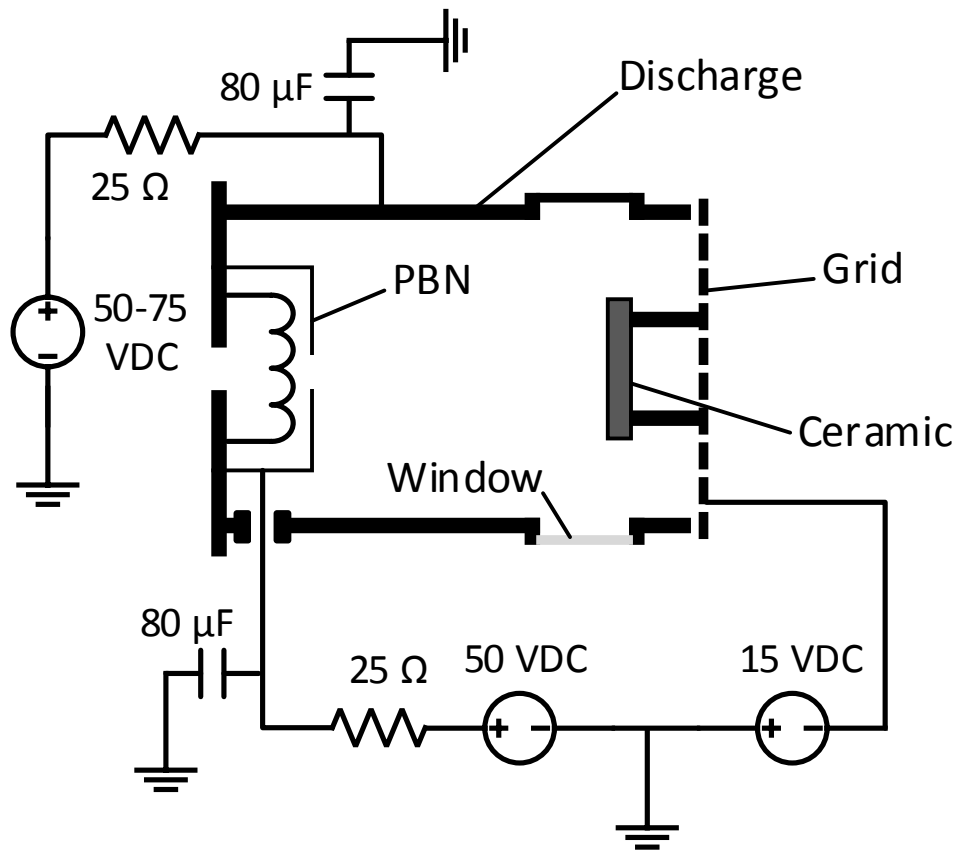
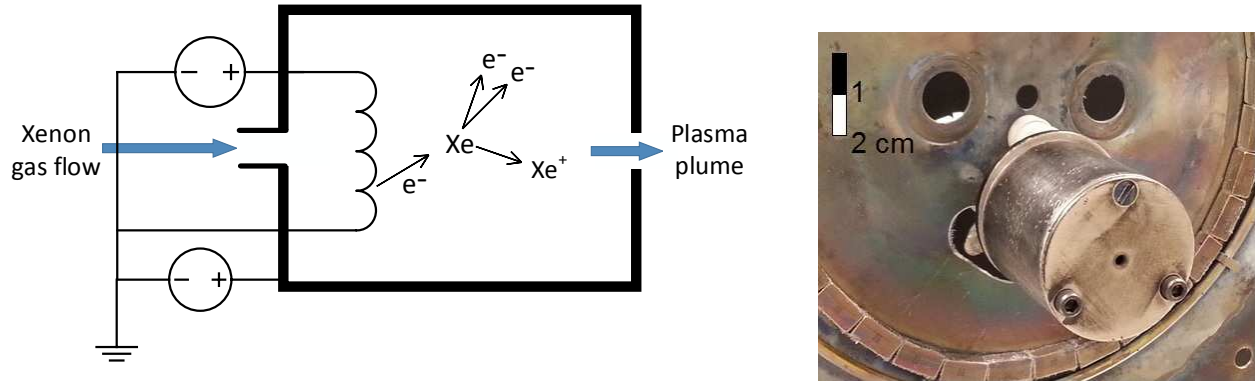


Figure 3.1: Top view diagram of the plasma source and accompanying wiring diagram (8 A filament supply and Langmuir probe not shown).



**Figure 3.2: Left: Diagram of a plasma bridge neutralizer showing hot tungsten filament thermionically emitting electrons to ionize neutral xenon. Right: Photograph showing the PBN mounted to the back wall of the discharge and the small central hole to allow the laser beam to enter the plasma source.**

electrons and draw ions. Mounted on the grid is the ceramic mount, which is electrically floating and holds the test material (boron nitride or alumina and sometimes molybdenum for verification purposes). The laser beam comes in through a small hole just above the PBN and strikes the ceramic (see Figure 3.2 and 3.1). The ceramic surface is not exactly perpendicular to the incident beam, rather it is slightly tilted ( $\sim 5$  degrees) towards the collection optics to ensure the solid angle subtended by the collection lens is minimally cut off by the ceramic itself while still measuring the desired ion velocity component with negligible error. An on-edge view of the ceramic is provided by a small windows (1.4 inch aperture) built into the discharge and chamber to allow for collection of the LIF.

Operation of the plasma source requires 4 different biased elements set to either a constant voltage or constant-current. The two elements with the most influence on plasma properties are the filament and the anode. The filament provides energetic electrons and is typically operated at a constant current of 8 amperes. The plasma is forced to occur between the anode and the filament and can be operated at a discharge current of 0.2 to 2 amperes (constant current) depending on the desired plasma condition. The plasma density measured with a Langmuir probe increases linearly with discharge current (and thus voltage) as shown in Figure 3.3. The Debye length is shown to also decrease as one over the square root of either the discharge current or the plasma density. The grid and PBN body are the other

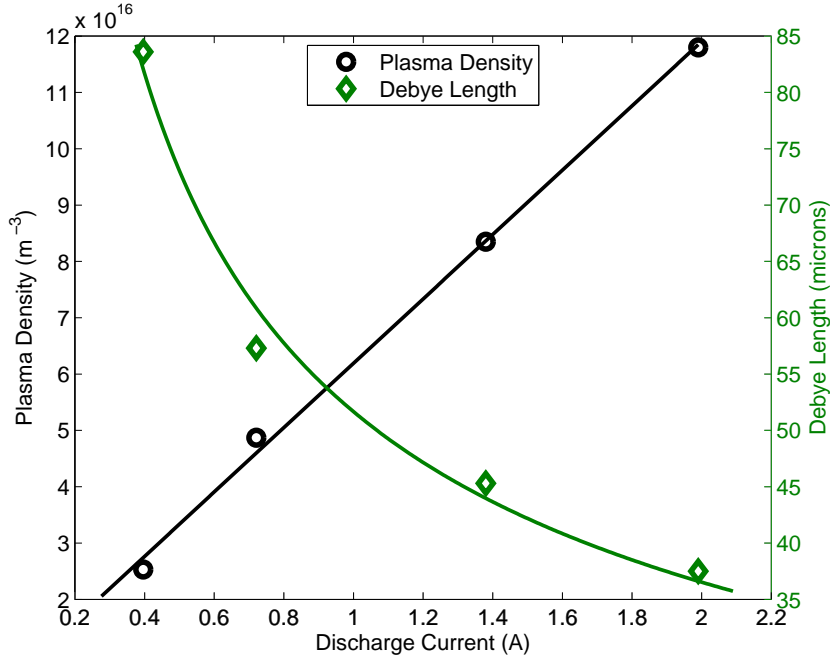


**Figure 3.3: Plot of plasma density and Debye length versus discharge current showing obtained data and best fits. Density is linearly related to discharge current and the Debye length is inversely related to the square root of discharge current and plasma density.**

two biased elements, operated in constant voltage and constant current modes, respectively. Ballast resistors are in-line to the PBN and discharge and have values of about 25 ohms each. In addition, two  $80 \mu\text{F}$  oil-filled capacitors are connected between the cathode (earth ground) and the anode of the discharge and PBN (see Figure 3.1). These capacitors are as close to the chamber feed-through as possible and in conjunction with the resistors are meant to stabilize the power supplies and plasma source. When operating at low density without these components in place, the plasma will rapidly jump between discrete plasma potentials causing unstable ion velocity distributions as evident by multiple recorded LIF peaks. The resultant voltage at the PBN and discharge due to the ballast resistors is approximately 10 V and 32-35 V respectively based on desired plasma conditions.

An added complexity of hot-filament discharges is the existence of so called primary electrons with a nearly monoenergetic energy distribution. Thermionically emitted electrons from the hot tungsten filament within the PBN have an energy equal to the potential differ-

ence between the PBN plasma and the discharge plasma, and are assumed to be isotropic (no directionality). Primary electrons that have lost energy (e.g. due to ionization collision with neutral xenon, bremsstrahlung, etc.) form a Maxwellian distribution of thermalized electrons, often called Maxwellian electrons. Depending on conditions, the primary density fraction ( $\alpha$ ) is about 5%, with an energy of  $\sim 20$  eV. These electrons present an added complexity because they have the potential to further complicate the sheath dynamics.

### 3.1.1 Langmuir Probe

To quantify important plasma parameters, a Langmuir probe is used and extends down from the top of the discharge directly above the beam path. The probe itself is a small exposed metal wire 0.25 in diameter by 3 mm protruding from a ceramic insulating sleeve. It is biased with respect to the plasma cathode from -30 to 60 volts using a power supply (TDK Lambda ZUP120-1.8) while probe current is measured using a desktop multimeter (HP 34401A). Ideally, these I-V data have three distinct regions called ion saturation, transition and electron saturation (as seen in Figure 3.4). Analysis of the current-voltage (I-V) curve

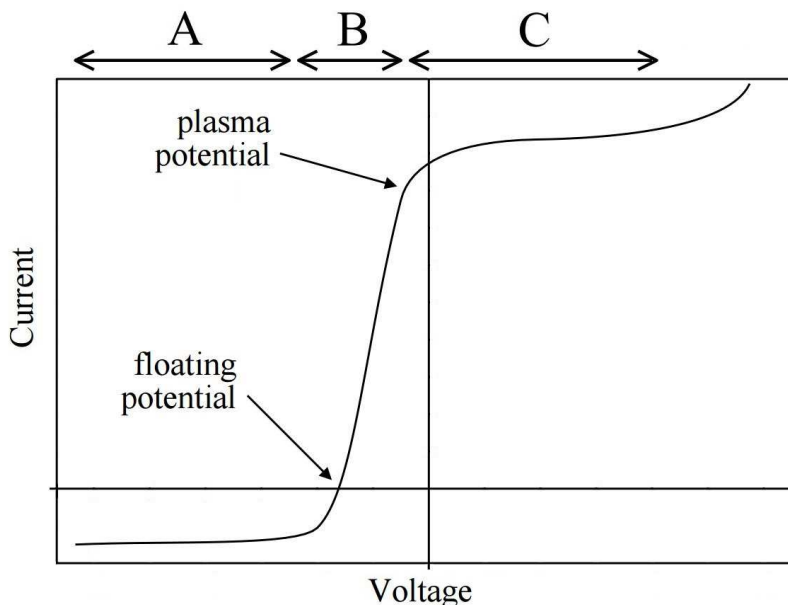


**Figure 3.4: Ideal I-V curve from a Langmuir probe in a plasma with negative floating and plasma potentials. Region (A) is the ion saturation region, (B) is the transition region, and (C) is the electron saturation region.**

over the three regions provides basic plasma parameters such as primary and Maxwellian electron temperatures and densities, as well as the plasma and floating potentials. If the applied probe voltage is too high and/or the probe area is too large, the current draw of the probe may be too large and be comparable with the discharge current of plasma source. This effect can be seen in Figure 3.4 where, at high voltage, the current increases beyond the electron saturation current. To minimize perturbation, the electron saturation current must be small compared to the anode (discharge) current.

As mentioned earlier, the primary electrons present in the plasma source affect the sheath dynamics. This effect increases the electron current at lower probe voltages, distorting the transition region and requiring a different analysis method than what would be typically used on the I-V curve in Figure 3.4. Total electron current,  $I_e$ , to a probe of known dimensions is given by

$$I_e = I_{ep} + I_{pri}, \quad (3.1)$$

where  $I_{ep}$  and  $I_{pri}$  are the plasma (Maxwellian) and primary electron currents, respectively. Variables  $I_{ep}$  and  $I_{pri}$  are piecewise functions<sup>80</sup> given by

$$I_{ep} = \begin{cases} \frac{1}{4}en_{ep}A_{pr}\sqrt{\frac{8kT_{ep}}{\pi m_e}}\exp\left(\frac{e(V_{pr}-\phi_p)}{kT_{ep}}\right) & V_{pr} \leq \phi_p \\ \frac{1}{4}en_{ep}A_{pr}\sqrt{\frac{8kT_{ep}}{\pi m_e}} & V_{pr} > \phi_p \end{cases} \quad (3.2)$$

and

$$I_{pri} = \begin{cases} \frac{1}{4}en_{pri}A_{pr}\sqrt{\frac{2E_{pri}}{m_e}} & V_{pr} > \phi_p \\ \frac{1}{4}en_{pri}A_{pr}\sqrt{\frac{2E_{pri}}{m_e}}\left(1 - \frac{e(\phi_p - V_{pr})}{E_{pri}}\right) & \left(\phi_p - \frac{E_{pri}}{e}\right) \leq V_{pr} \leq \phi_p \\ 0 & V_{pr} \leq \left(\phi_p - \frac{E_{pri}}{e}\right) \end{cases} \quad (3.3)$$

where  $A_{pr}$  is the probe area,  $V_{pr}$  is the probe voltage,  $n_{pri}$  is the primary electron density,  $n_{ep}$  is the plasma electron density,  $E_{pri}$  is the primary electron energy in joules and  $T_{ep}$  is the

plasma (Maxwellian) electron temperature. In the transition region  $(\phi_p - E_{pri}/e) \leq V_{pr} \leq \phi_p$  Equation 3.4 describes the total electron current to the probe as

$$I_e = \frac{1}{4}en_{ep}A_{pr}\sqrt{\frac{8kT_{ep}}{\pi m_e}}\exp\left(\frac{e(V_{pr} - \phi_p)}{kT_{ep}}\right) + \frac{1}{4}en_{pri}A_{pr}\sqrt{\frac{2E_{pri}}{m_e}}\left(1 - \frac{e(\phi_p - V_{pr})}{E_{pri}}\right). \quad (3.4)$$

One can solve for all the unknown plasma parameters in Equation 3.4 when this equation is fit to the I-V data in the transition region. Shown in Figure 3.5 is an example of a partial I-V curve and fit to the data are Equation 3.4 over the applicable bounds of  $(\phi_p - E_{pri}/e) \leq V_{pr} \leq \phi_p$ . The fit departs from the data at the plasma potential (the 'knee' in the data, near 33 V), where the probe is negative enough to repel the primary electrons. The plasma parameters resulting from the fit in Figure 3.5 are:  $T_{ep} = 2.5$  eV,  $E_{pri} = 28$  eV,  $n_{ep} = 1.5 \times 10^{16} m^{-3}$ ,  $n_{pri} = 1.2 \times 10^{15} m^{-3}$ ,  $\phi_{floating} = 19$  V and  $\phi_p = 33$  V. From these data, the Bohm velocity and Debye Length can be calculated as  $u_B = 1400$  m/s and  $\lambda_D = 94 \mu m$ , respectively. To put the electron temperatures into context, neutral xenon has a minimum ionization energy of 12.13 eV and the ionization cross section peaks at about 70 eV.<sup>81,82</sup>

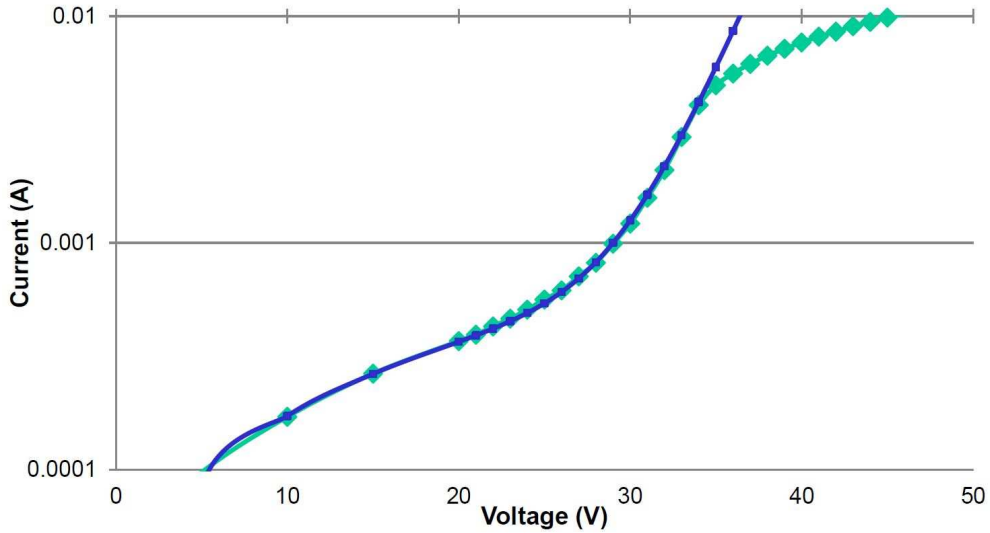


**Figure 3.5:** Experimental I-V data from the Langmuir probe (green), plotted with a logarithmic vertical axis and Equation 3.4 in blue.

In situations where there are is a bi-Maxwellian population of plasma electrons, an effective temperature (harmonic mean) of the cold and hot electrons must be calculated to accurately determine other quantities. Researchers Severn et al.<sup>16</sup> and others<sup>19,83</sup> make use of the effective temperature to better describe the plasma. In this work, primary electrons are typically 3-6% of the electron density, at a relatively low energy, and therefore have a small effect on the effective temperature. For this reason, only the Maxwellian electron temperature is used to determine such quantities such as Debye length and Bohm velocity.

## 3.2 LIF Scheme and Experimental Setup

### 3.2.1 LIF Scheme

The laser-induced fluorescence scheme in this work utilizes a metastable state of singly ionized xenon (commonly denoted as Xe II or Xe<sup>+</sup>). Photoexcitation via a 834.953 nm wavelength photon excites an electron from the  $5d[4]_{7/2}$  energy level to the  $6p[3]_{5/2}$  energy level. This process excites xenon into an unstable configuration and spontaneously decays to the  $6s[2]_{3/2}$  energy level approximately 9.3 ns later.<sup>84</sup> The decay process releases more energy than was originally absorbed, emitting a photon of wavelength 542.066 nm in vacuum (see Figure 3.6). This type of scheme is known as non-resonant, which allows for easy discrimination between scattered laser light and fluorescence using a simple bandpass filter such as a monochromator.

Ions with a non-zero velocity component in the axis of the laser wave vector will absorb at a different frequency than a stationary absorber. This phenomenon is known as the Doppler effect and shifts the absorbing frequency by  $\Delta\nu$  according to

$$u_i = \frac{c\Delta\nu}{\nu_0 + \Delta\nu} \approx \frac{c\Delta\nu}{\nu_0} = \lambda_0\Delta\nu, \quad (3.5)$$

where  $u_i$  is the ion velocity in the axis of the laser beam,  $c$  is the speed of light,  $\Delta\nu$  is the change in observed frequency and  $\nu_0$  and  $\lambda_0$  are the center transition (non-Doppler shifted)

frequency and wavelength, respectively. A positive value of  $u_i$  travels with the light and is known as blueshifted, and conversely, a negative  $u_i$  produces a redshifted result.

### 3.2.2 LIF Saturation

The resultant LIF signal is not a sharp peak from a population of monoenergetic ions traveling in the same direction, rather it is a Gaussian-like distribution that is broadened by multiple mechanisms. Laser lineshape, Doppler effect, hyperfine structure and other less significant broadening factors all contribute to the finite width of the LIF spectrum. While these are unavoidable broadening mechanisms, saturation broadening can be prevented. A LIF signal that is as strong and narrow as possible aids in the ability to distinguish it from the noise. This is especially important when measuring further and further into the sheath where the reducing ion density decreases the signal-to-noise ratio (SNR). If the laser is operating in the saturated LIF regime, the signal intensity (for a given volume of plasma) is maximized and independent of laser irradiance. In this situation, the population of Doppler shifted ions matching the absorption frequency corresponding to the peak of the laser lineshape will saturate first. If laser intensity is increased beyond the onset of saturation, a broader range of the ion population will begin to saturate and the wings of the LIF signal will increase in

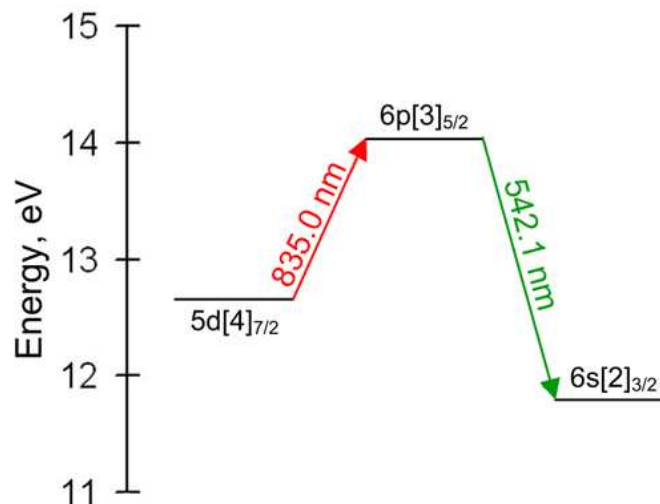
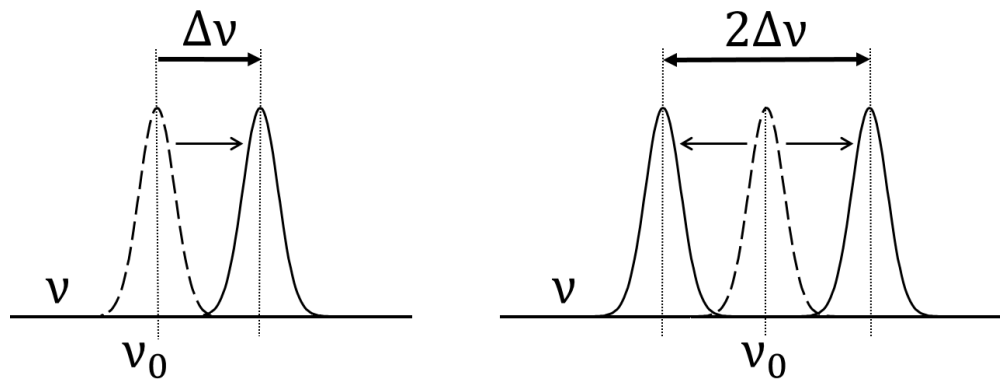


Figure 3.6: Transition diagram of Xe II denoting approximate photon wavelengths in vacuum, adapted from.<sup>84</sup>

intensity due to the finite laser linewidth. Then, if the laser is scanned across the spectral line, the broadening is worsened as the intense peak frequency is scanned across the entire ion velocity distribution function (IVDF). This effect distorts the IVDF by artificially increasing the full width at half maximum of the LIF signal. By tuning the laser power just below the point of saturation, the LIF is said to be in the linear regime where signal intensity is linearly related to laser pump intensity. Thus operating in the linear regime eliminates this broadening mechanism and aids in detecting a poor signal in a high noise environment.

### 3.2.3 Sheath Potential Calculation

Conveniently, the incident laser light diffusely reflects off the ceramic surface and the ions consequently observe a redshifted transition. The result is two Doppler shifted transitions and therefore the ion velocity is related to half the total frequency spacing between the two peaks as shown in Figure 3.7. This reflected light is not a perfect specular reflection and therefore further Doppler broadens the reflected LIF spectrum. While this effect is noticeable, it does not affect the measurement, as only the most probably velocity corresponding to the maximum florescence signal is used. Intensity of the LIF from the reflected beam at peak absorption is significantly lower compared to the incident, suggesting the laser intensity is lower, but the peak is still well defined as shown in Figure 3.8. Converting the calculated velocity to electric potential is a matter of manipulating conservation of energy. Using the



**Figure 3.7:** Doppler shifted LIF representation of a traditional single peak (left) and dual peak from incident and reflected laser light (right).

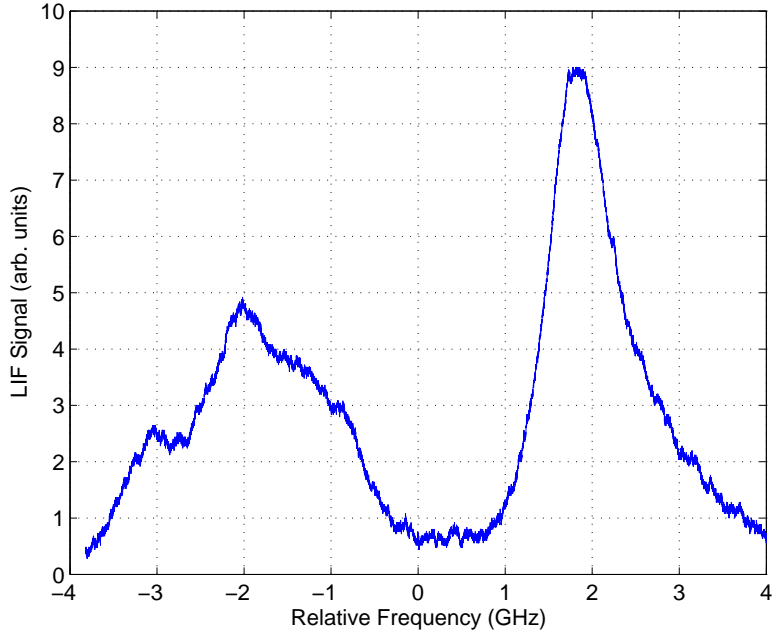


**Figure 3.8:** Experimental LIF data from the presheath surrounding a ceramic test piece showing the dual peak signal. The incident beam produced the narrow signal (right) and the reflected laser light produced the broad signal (left).

Bohm velocity (Equation 1.7) as the reference point, the relative sheath potential can be calculated. Conservation of energy given as

$$\frac{1}{2}Mu_i(x)^2 = \frac{1}{2}Mu_B^2 - e\phi(x) \quad (3.6)$$

where the final ion kinetic energy is equal to the initial ion kinetic energy plus the gained potential energy. Solving for  $\phi(x)$ , gives

$$\phi(x) = \frac{M}{2e} (u_B^2 - u_i(x)^2) \quad (3.7)$$

where  $\phi(x)$  is the the local sheath potential relative the sheath edge.

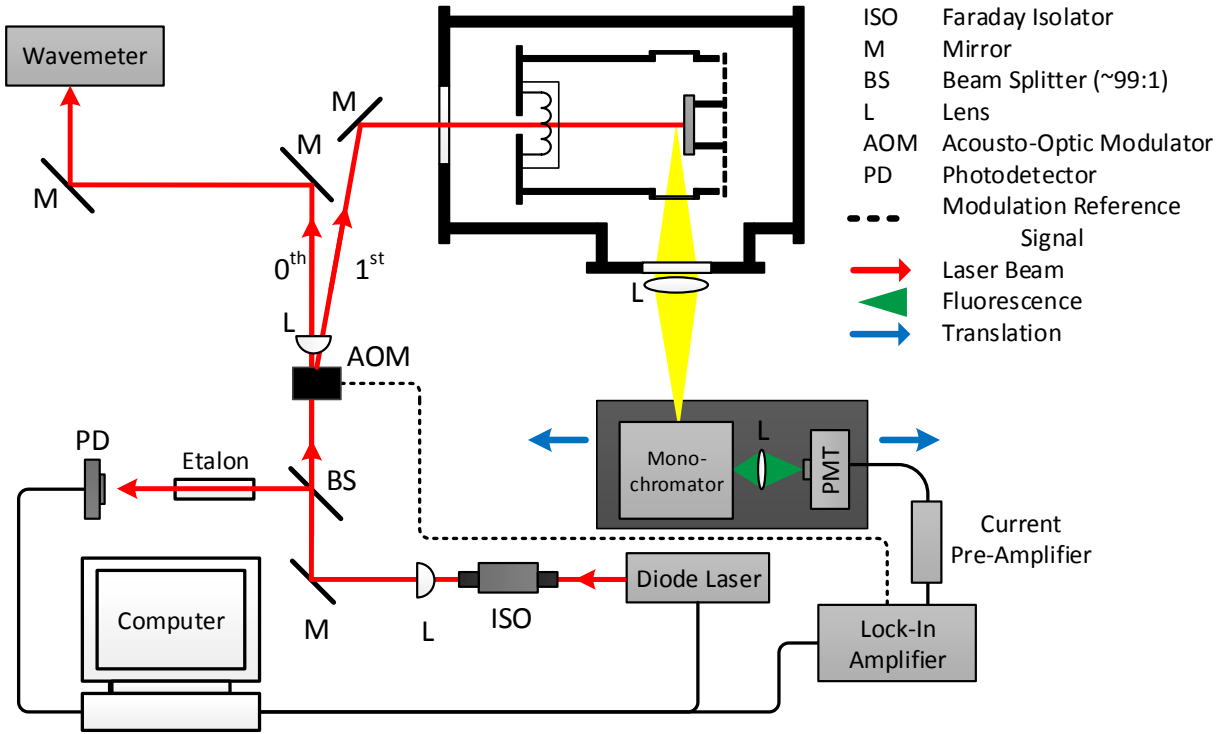


Figure 3.9: Schematic diagram of the experimental setup including the plasma source.

### 3.2.4 Experimental Setup

Many instruments and pieces of equipment must be operated simultaneously to measure the Doppler shift of ions traveling through the sheath, to calculate the velocity and electric potential. Figure 3.9 shows a schematic diagram of the experimental setup used in this work. The following paragraphs of this subsection describe each piece of equipment and how it is used for measuring xenon ion velocity.

The laser shown in Figure 3.9 is an external cavity diode laser (Toptica DL100) with a maximum mode-hop free scanning range of 22 GHz, near 835 nm with a maximum output power of approximately 50 mW. To prevent unwanted back reflections from feeding into the laser and altering the wavelength, the beam immediately passes through a Faraday isolator (Isowave I-7090C-L). To measure the laser frequency scan rate, a small portion of the laser power is fed into a fabry-perot interferometer via a beamsplitter. This type of interferometer is also known as an etalon and it has a free spectral range (FSR) of 2.31 GHz. As the laser

light frequency varies with time, it constructively and destructively interferes (alternating every half FSR) in the cavity and produces a sinusoidal like signal from the photodiode (Thorlabs PDA10CS) at the exit, which is used for relative frequency calibration. Further down the beam path, light is fiber coupled into a wavemeter (Coherent WaveMaster) which is used for coarse tuning and wavelength monitoring.

Prior to the etalon, a 500 mm cylindrical lens is used to focus the elliptical beam in order to pass the light through an acousto-optic modulator (AOM, NEOS 23080-1). As the laser beam passes through the crystal material inside the AOM, pulsing sound waves propagating in the media deflect the beam at a specified frequency and duty cycle, creating the modulated 1st order shown in Figure 3.9. The undeflected 0th order and 1st order beams are recollimated by another 500 mm cylindrical lens placed two focal lengths downstream of the first cylindrical lens. The modulation frequency is controlled by a function generator which outputs a 2 kilohertz square wave signal to the AOM and the lock-in amplifier (EG&G 5210).

The 1st order beam then enters the chamber via a window (N-BK7 glass, anti-reflective coated for near-infrared light), and into the plasma source where it strikes the ceramic plate. At this position, a few meters downstream of the laser head, the beam has expanded to a diameter of about 4 mm. With a pump power of about 20mW, this is approximately the minimum size that will not saturate the LIF. At a right angle to the beam are two more windows, on the plasma source and the vacuum chamber to allow LIF collection from ions near the ceramic surface. Both windows are N-BK7 glass but only the chamber window is anti-reflective coated for visible light (LIF is green light) due to the extreme temperatures from the plasma in contact with the first window. The collection volume is imaged onto a monochromator (EG&G PARC 1229) with an entrance slit of 120 microns wide, using a 2 inch diameter 200mm focal length spherical lens. The imaging is setup to magnify at a 2:1 ratio, which doubles the spatial resolution from 120 microns to 60 microns along the beam path, but at the cost of halving the collected LIF power. The filtered light exiting

the monochromator (542 +/- 1 nm) passes through a 25 mm lens to focus the LIF into a photomultiplier tube (PMT, Oriel 77340). Operated at about -520 V the PMT amplifies the signal by about  $10^5$  A/W. The output current from the PMT then sent to a current preamplifier (Femto DHPKA-100) where the signal is converted from a current signal into a voltage signal and further amplified by  $10^7$  V/A.

Because the laser beam is being modulated at 2 kilohertz, so too is the LIF. The current signal from the current preamplifier is sent to a lock in amplifier in order to pick out the LIF signal and reduce nearly all of the noise. Lock-in amplifiers work by using phase sensitive detection to pick out a signal that is at the reference frequency and phase. As mentioned earlier the AOM modulates the pump beam, and therefore the LIF, is operated using the same reference frequency as the lock in amplifier. Ultimately, this allows for detection and isolation of the weak LIF in an extremely high noise environment. The signals from the LIA, photodiode and laser controller are all sent to an oscilloscope and processed in MATLAB (discussed in section 3.3).

### 3.2.5 Experimental Limitations

As stated in section 1.3.2, there are general limitations to LIF as a plasma sheath diagnostic tool. For this experiment, a significant limitation is the indeterminate location of the measurements. As measurements are taken closer and closer to the ceramic, the LIF signal strength decreases to a point where it is indistinguishable from the noise. It was initially thought that, this location where the signal "dies" is roughly the surface of the ceramic, where ions do not exist. After careful thought it was realized this location is *only* where there is insufficient LIF intensity reaching the detector to exceed the noise and is not necessarily the plasma-wall boundary. Insufficient LIF could be due to one or more of the following: low ion density, too broad of an LIF spectrum to distinguish from the noise, or the solid angle subtended by the collection lens being cut off by the proximity of the ceramic. Excited xenon suffering from quenching (i.e. collisional de-excitation preventing fluorescence), is not thought to be significant since the sheath is largely collisionless.

If the sheath electric field induces a high velocity compared to the Bohm velocity, ion density could decrease below the detection limit prior to reaching the wall. In this case, only a partial measurement of the entire sheath potential profile would be possible using this LIF scheme. An experiment was devised to test this theory. By replacing the ceramic with a molybdenum sheet, the wall could be biased above or below the floating potential, directly affecting sheath voltage and the final velocity of the ions before impact. The wall was first forced to the floating potential ( $\sim 10$  V), and the collection stage was moved to collect LIF further and further into the sheath and set to the position where the LIF signal became immeasurable compared to background. The molybdenum wall was then biased 5V above the floating potential ( $\sim 15$  V) and suddenly the instruments were collecting a strong and repeatable LIF signal due to a higher ion density. At this higher wall potential, the new location where the signal dies was several hundred microns closer to the wall. With the theory confirmed, it solidified the hypothesis that the absolute location of the measurements is unknown. To devise a way of repeatably measuring the location of the wall (with an accuracy much greater than the resolution of the collection optics), and relating it to the location of the collection stage, was deemed beyond the scope of this project. Every time the vacuum chamber was opened for maintenance or an experimental change, the location of the wall was moved, which was the root of the problem and completely unavoidable.

Researchers Severn et al.<sup>16</sup> were also unable to measure ion velocity very near the wall using LIF. However, their measurement position was estimated using the Child-Langmuir model to calculate the sheath thickness. As discussed in section 1.2, a sheath meeting the criteria of  $e\phi_s \gg kT_{ep}$ , is assumed to be electron and presheath free and has a thickness given by Equation 1.10. By doing so, Severn et al. discovered that ion velocity measurements were only possible in roughly half the sheath (the half closest to the bulk plasma). Based upon the typical plasma parameters measured in this work by a Langmuir probe, the ratio of sheath voltage to electron temperature ( $e\phi_s/kT_{ep}$ ) is about 5, compared to 29 in the work of Severn et al.

The second significant experimental limitation is the laser and laser controller. It is *the* limiting factor in the quality of the data. Averaging as many scans together as practical and scanning at the slowest possible rate (allowing a high LIA time constant) are obvious methods to improve the capability of this diagnostic technique. Unfortunately, the temporal stability of the laser system does not reliably allow for more than two scans per measurement position. The laser is in need of constant adjustment due to mode-hopping and wavelength drifting which frequently interrupts and resets a data set, significantly slowing the process of measuring the entire sheath. Given the age of the laser and the less than ideal conditions of the building housing the laboratory, the quoted maximum scan range of 22 GHz, is not achievable. The largest mode-hop free scan range attained after taking apart and realigning the laser was 18 GHz, which lasted for a mere 10 minutes and is the range needed for the expected ion velocity very close to the wall. Reattaining any desired scan range after a mode-hop frequently requires a significant readjustment of the operating conditions of the laser. This invariably includes changing the driving current to the diode, altering the power output, which is obviously undesirable when operating near the limit of the linear regime to maximize LIF power and the sheath measurement depth. In summary, laser instabilities are exacerbated by longer operating times and larger scan ranges that effectively limits the type of measurable sheath (to a relatively small sheath voltage causing low ion velocity), the total number of measurement positions and the amount of scans taken per measurement position.

### **3.3 Data Processing Method**

The data streams needed to calculate xenon ion velocity and the sheath potential profile include the LIF signal from the lock-in amplifier (LIA), relative frequency measurements from the photodiode and the trigger signal from the laser controller. All three of these are fed into a oscilloscope (Tektronix TDS 5034B) and saved to a flash drive. Raw data shown in Figure 3.10 is from two complete laser scan periods consisting of two up- and down-scans each in frequency space. The laser scan control module (SC110) is set to scan with the

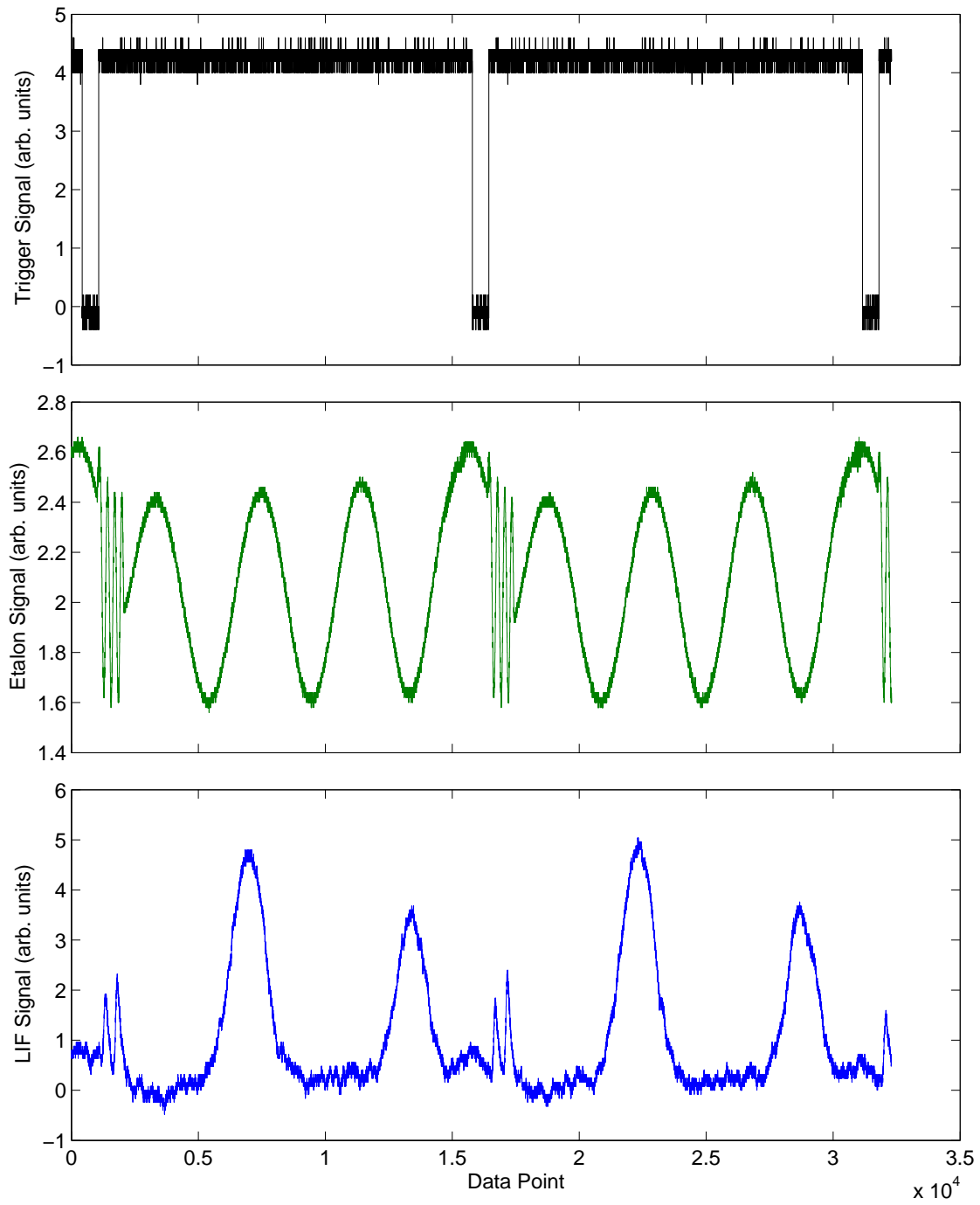


**Figure 3.10:** Raw experimental data from laser controller (top), etalon (middle), and LIF (bottom) collected from a sheath surrounding a molybdenum test piece. From left to right, it consists of two complete scans starting with a fast up-scan, followed by a slow down-scan and repeated once more (with small portions of extraneous data at the beginning and end).

longest possible period and to further minimize the scan rate (of either up- or down-scan), it is set up to scan at an asymmetric rate.

In each data set throughout this work, the down-scan is approximately 90% of the scan period, and 285 seconds long. The up-scan can easily be spotted (and conversely the down-scan) in Figure 3.10 where the frequency of the etalon signal is much higher and also corresponds to the tightly grouped, small LIF peaks. By using this scan technique, it renders the up-scan LIF data unusable, but it is a minor inconvenience to waste roughly 10% of the total scan time.

As noticed in Figure 3.10 the second LIF peak in each down-scan is smaller and lower in frequency within the scan. It corresponds to the redshifted absorption from the reflected beam. It is considerably different from the same peak in Figure 3.8 when compared to their blueshifted counterparts. The data in Figure 3.10 is collected from sheath surrounding a semi-polished molybdenum test piece where the laser beam is reflected more specularly and thus produces a signal that is less Doppler broadened. Using molybdenum as a ceramic

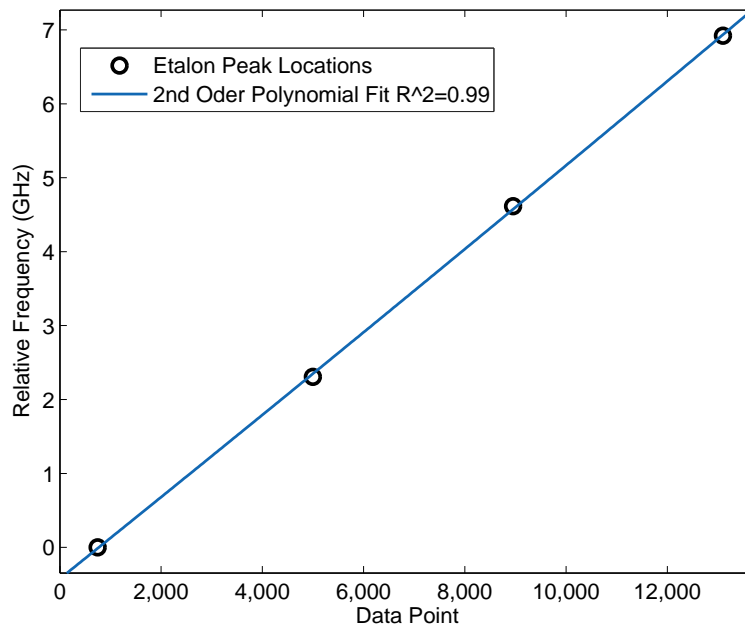


**Figure 3.11: Graph of the etalon peak locations with a second order polynomial fit.**

surrogate easily provides a way to verify the measurement technique by biasing the moly plate and producing known sheath characteristics. For example, if the moly was biased to the plasma potential, in theory, no sheath would exist and ions would not experience an accelerating electric field and remain at a constant velocity.

Processing the data in MATLAB is fairly straightforward, especially with the laser trigger signal. This signal provides a consistent location of where to cut the LIF and etalon data arrays into separate full scans. Then the up-scan is selected and discarded as it makes up a consistent 10%, at the start of each full scan. This percentage is a constant regardless of scan range because the scan period is constant with respect to scan range, but the scan rate is not. With each array properly trimmed to equal lengths, the etalon signal is analyzed to provide a calibrated frequency axis. The array is smoothed and the location of the peaks, where constructive interference is maximum, are recorded. Knowing these points are spaced exactly one FSR (2.31 GHz) apart, a second order polynomial is fit to these points as seen in Figure 3.11. The scan rate is not constant over the entire range, and becomes more apparent

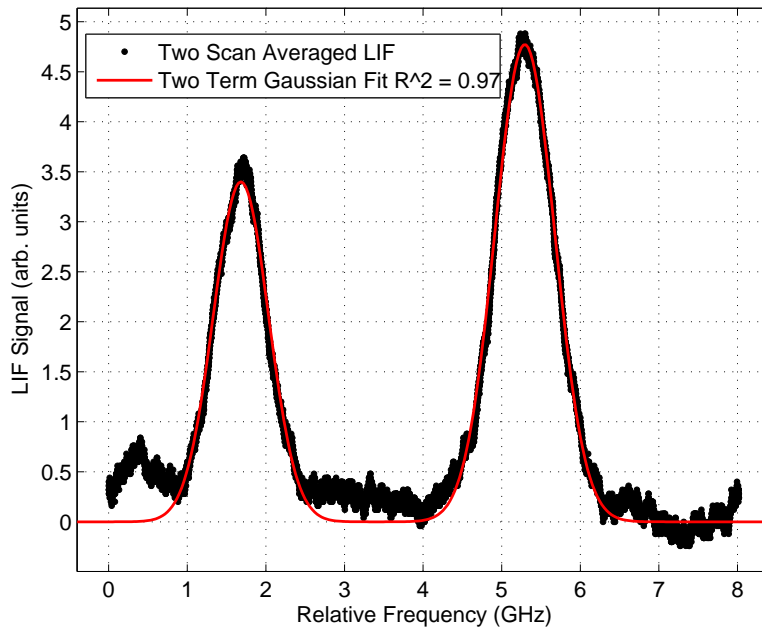


**Figure 3.12: Graph of an averaged LIF signal with a two term Gaussian fit resulting in a  $2\Delta\nu$  of 3.61 GHz.**

for large scan ranges, hence the need for a non-linear fit. This equation relates data points of the trimmed arrays to a relative frequency in gigahertz.

The LIF down-scans are combined and averaged where Gaussian lineshapes are fitted to both peaks with the calibrated frequency axis, shown in Figure 3.12. This method provides the frequency separation of the peak locations which is equal to twice the Doppler shifted frequency and can be converted directly to ion velocity using Equation 3.5. With measurements taken across the presheath and sheath at the desired resolution, the measured ion velocity can be converted to a relative potential with respect to the sheath edge using Equation 3.7. The resulting sheath potential profile from this data set is discussed in the next chapter.

### **3.4 Optimization Techniques**

As previously mentioned, improving the signal-to-noise ratio (SNR) is the key factor enabling high resolution measurements deep within the sheath. Optimizing the experiment for maximum SNR was accomplished by maximizing the fluorescence and collection efficiency, minimizing sources of noise and optimizing the signal processing equipment. The approximate benefit from the following changes increased the SNR by a factor of  $\sim 200$ , which has been ultimately traded for higher resolution measurements.

#### **3.4.1 Signal Improvement**

To improve the fluorescence signal, there are basically two separate avenues to explore. One can change how the laser light interacts with the plasma, by altering the pump power, intensity, and/or shape of the beam. The second method is improving the collection efficiency by increasing the amount of collected LIF.

A simple way to boost the signal is done by increasing the diameter of the collection lens, the lens that images the interrogation region onto the monochromator slit. This idea was originally dismissed because it was thought to equally increase the noise and signal, producing no net SNR benefit. While it is true a larger lens would collect more signal

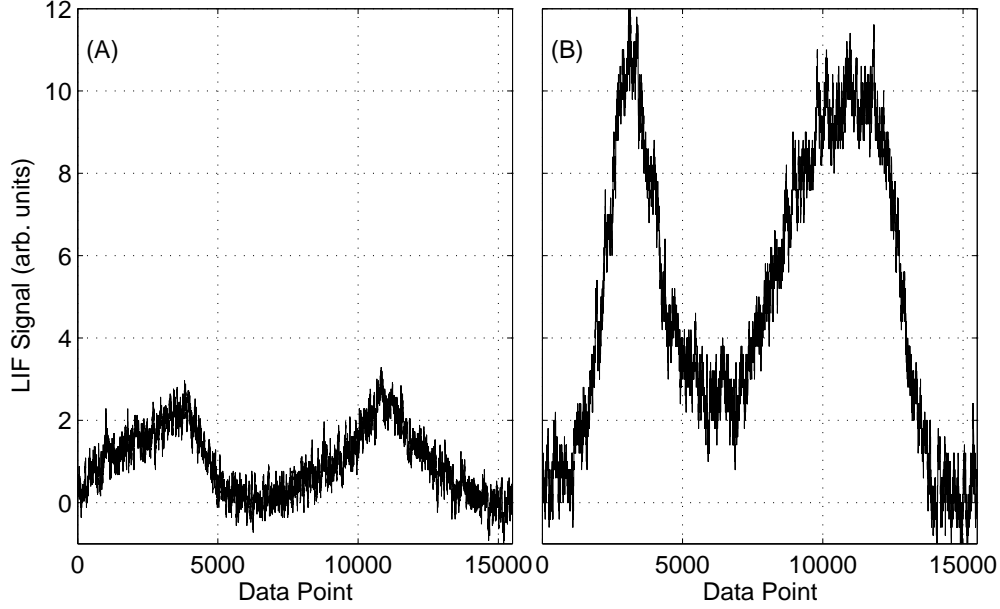


**Figure 3.13: Plots showing relative difference between 1 inch (A) and 2 inch (B) collection lenses. Both data sets are taken at identical plasma and operating conditions.**

and noise, assuming the noise is random, it will add in quadrature (rather than the simple summation a DC signal undergoes) resulting in a net SNR gain. As shown in Figure 3.13, doubling the collection lens diameter, increased the signal significantly more than the noise. The effect of quadrupling the lens area roughly quadrupled the peak LIF signal (from  $\sim 2.7$  to  $\sim 11$  arbitrary units) and the resultant SNR doubled (from about 10 to 20). Further scaling of collection optics is limited by the 2 inch chamber window.

Another significant improvement that increased the LIF signal was a larger final beam diameter allowing for more pump power. The experiment was originally equipped with a final focusing lens ( $f = 1$  m) in the beam path immediately before the chamber. This lens weakly focused the beam onto the ceramic and by doing so, it limited the maximum LIF intensity due to saturation. Removing the lens caused the beam to expand (from roughly 2 mm to 4 mm), thus reducing the pump intensity, which allowed for a higher pump power while still staying in the linear regime. A higher overall pump power increased the LIF power reaching the detector as seen in Figure 3.14. The limiting factors of further increasing the

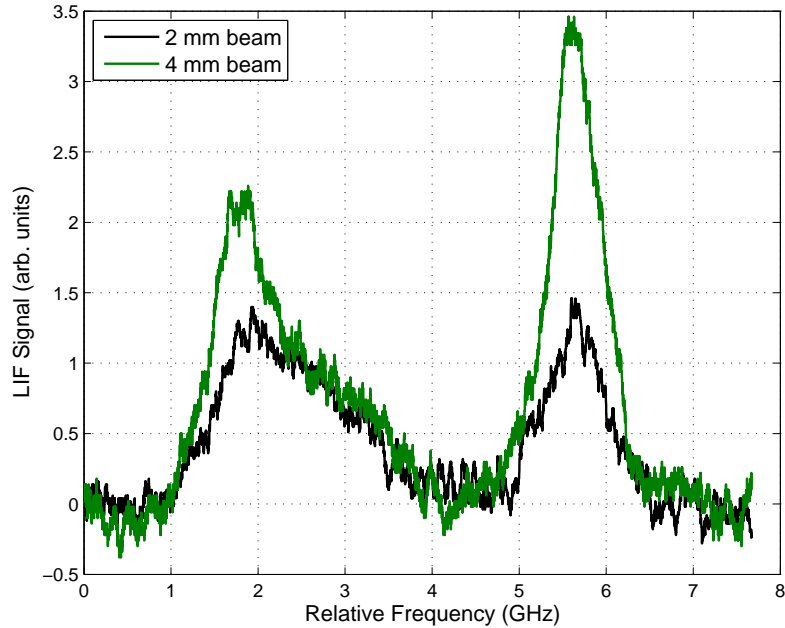


**Figure 3.14: LIF signal improvement from removing the final focusing lens which doubled beam diameter from roughly 2 mm to 4 mm, allowing for more pump power.**

final beam diameter are the depth of field of the imaging optics and the spatial variation in plasma properties causing non-uniform sheaths.

### 3.4.2 Noise Reduction

One of the most significant improvements came from replacing the exposed filament with a plasma bridge neutralizer (PBN). An exposed filament was originally used in the plasma source and in order to effectively emit ionizing electrons it must be hot enough to do so and consequently a significant portion of the blackbody radiation is in the visible spectrum along with the LIF. Containing the filament in a small metal can blocks the majority of the light, thus reducing the amount of unwanted light from reaching the detector. Shown in Figure 3.15, the noise was reduced significantly, which increased the SNR by a factor of 6 (from  $\sim 10$  to 60).

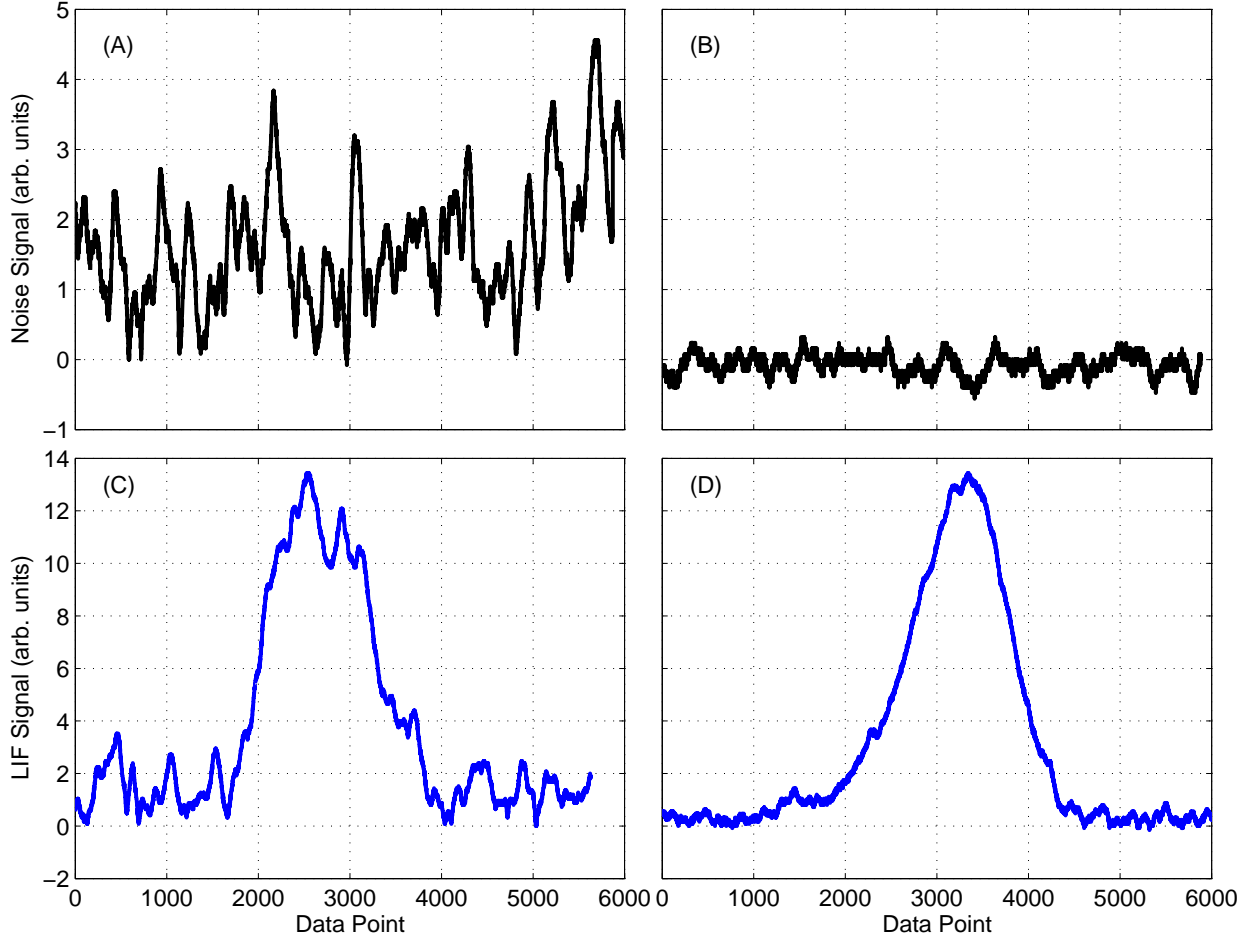


**Figure 3.15:** Plots of noise (top row, absent of LIF) and LIF (bottom row) with and without the plasma bridge neutralizer (PBN). Plots (A) and (C) are prior to installation, (B) and (D) are after.

### 3.4.3 Signal Processing Optimization

Early on in the development of this experiment, an optogalvanic cell (Hamamatsu L2783-42 XeNe-Mo) was used for the absolute frequency calibration. This method requires a second LIA and forces them both to have a small integration time (time constant) of 100 ms to prevent temporal distortion and preserve the accuracy of the calibration.

By taking advantage of the self-calibrating nature of the dual peak method, it removed the need for the optogalvanic cell and the second LIA. The benefit of operating with one LIA is that the time constant can be set to a relatively high value that significantly improves the signal-to-noise ratio, allowing for measurements not otherwise possible. There is no interest

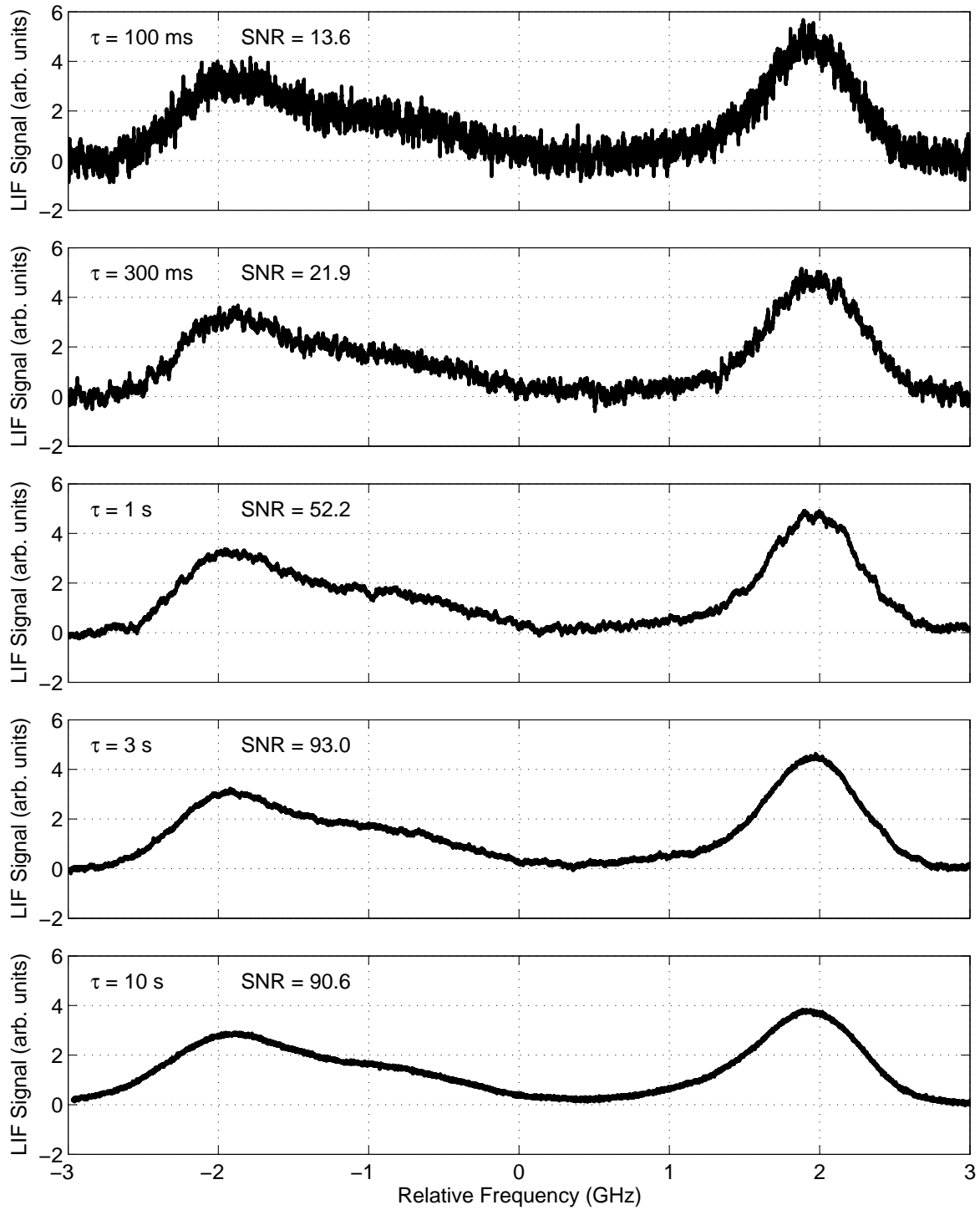
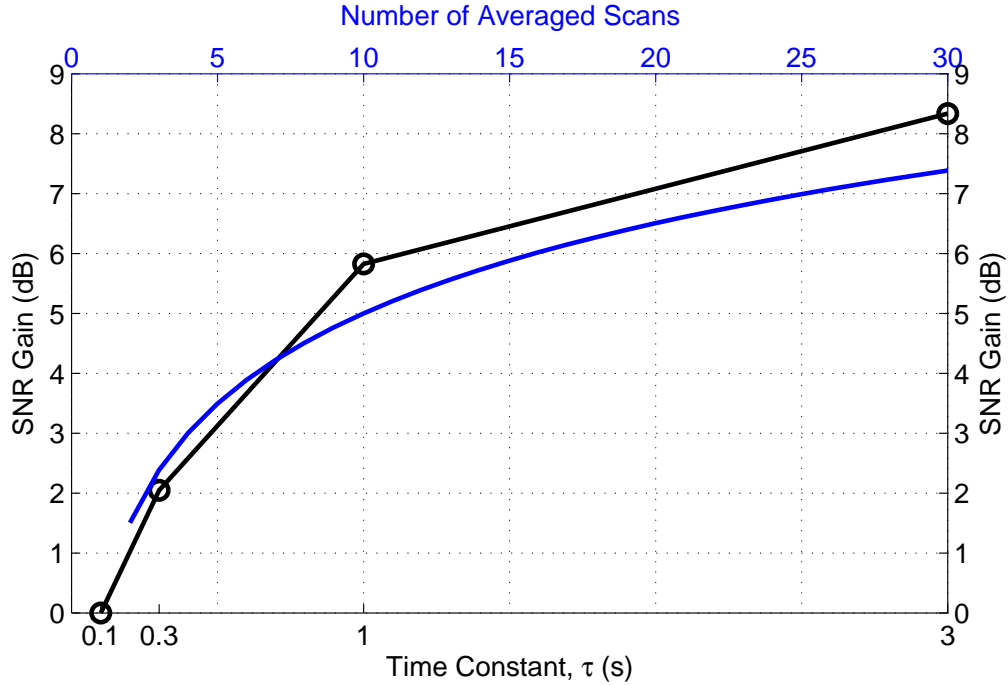


Figure 3.16: Plots of constant position LIF scans (2 averaged scans per plot) with varying lock-in amplifier time constant, as indicated.

in time resolved measurements in this work, so a temporally distorted LIF signal is not an issue, so long as each peak is distorted equally, thus maintaining the frequency separation.

Shown in Figure 3.16 is a data from a study to measure the effect of LIA time constant on peak separation and SNR. Each plot is an average of two down-scans with an average frequency separation across all 10 scans of 3.92 GHz with a standard deviation of 0.027 GHz. This standard deviation corresponds to a negligible velocity of  $\sim 10$  m/s at the 835 nm xenon transition. However, there is a significant reduction in signal strength when moving from  $\tau = 3$  s to  $\tau = 10$  s, which causes a drop in the SNR from 93.0 to 90.6. A time constant of 10 s too large compared to the measurement time of a typical LIF trace. The DL100 scan control module (SC 110) can scan the laser at a minimum of 3 mHz ( $\sim 300$ s period) for any given frequency scan range. Depending on the measurement location in the sheath (peak frequency separation), it will require different scan ranges causing the signal measurement time to vary roughly between 70 and 90 seconds (approximately the half period of the signal waveform). It was decided and shown experimentally, an integration time of 10s is too large compared to the signal measurement time which artificially decreased the signal strength too much for the amount of noise reduction, shown by the drop in SNR. In summary, the minimum scan period of the laser controller has limited the lock-in amplifier time constant to a maximum of 3 seconds to optimize the signal-to-noise ratio.

An alternative method to increase the SNR is to operate at a very high laser scan rate to take advantage of the scan averaging. Determined by my predecessor, Jordan Rath, signal averaging increases the SNR by approximately the square root of the number of averaged scans. Comparing this expected increase with the time constant study data shown in Figure 3.16 (with averaging effects removed) results in what is shown in Figure 3.17. The black data in Figure 3.17 is compared to one scan of LIF at  $\tau = 100$  ms with an SNR of 9.6. For example, increasing the time constant to 300 ms, gives a gain of 2 dB over 100 ms. The blue curve is simply the square root of the number of averages, however, the corresponding top horizontal axis is scaled to reflect the equivalent number of achievable scans during the



**Figure 3.17: Comparison of SNR gain of two methods, increasing time constant (black) and increasing number of averaged scans (blue), over an equivalent elapsed time.**

same time required for 1 scan at a given time constant. For example, at a 3 s time constant which requires a scan period of 270 seconds (based on the data shown in Figure 3.17) and in the same amount of time, 30 scans at 100 ms and 9 seconds each can be averaged, therefore the SNR gain from 30 averaged scans is 7.4 dB. Similarly, at 300 ms time constant requires a minimum scan period of 27 seconds, which is three times longer than a minimum scan period required for 100 ms, therefore 3 scans can be averaged in the same amount of time, giving a SNR gain of 2.4 dB. This is all assuming the that 270 seconds is the optimal time for a 3 second time constant, in other words, it assumes the optimal scan period is 90 times greater than the time constant. However, what ultimately matters is the ratio of signal measurement time (time required to measure an entire LIF waveform) to the time constant. A time constant that is much much less than the signal measurement time is advantageous to account for the variation of scan ranges throughout the entire test.

The question then becomes, what is the best way to further increase the SNR? As discussed, increasing the time constant from 3 s to 10 s decreases the SNR. Therefore, signal

averaging becomes better than one scan at  $\tau = 3$  s when more than 46 scans are averaged. However, the best method is a hybrid of high time constant and high averaging because at 60 averaged scans, an equivalent of two  $\tau = 3$  s scans can be averaged resulting in an additional gain of 1.5 dB on the 8.3 dB (= 9.8 dB) which is greater than averaging 60,  $\tau = 100$  ms scans (1.5 dB + 7.4 dB = 8.9 dB).

## 4 Results and Discussion

### 4.1 Demonstrative Sheath Measurement

Data from Figure 3.10 along with 9 other data sets were combined to show the potential and velocity variation within the sheath and presheath, shown in Figure 4.1. As expected, the potential in presheath (positive side of horizontal axis) is relatively constant. Discussed in section 1.2, the presheath thickness is set by the ion mean free path, or the chamber radius. In this experiment, the plasma source radius (10 cm) is much much smaller than the ion mean free path, which is on the order of meters. Therefore the entire presheath is  $\sim 10$

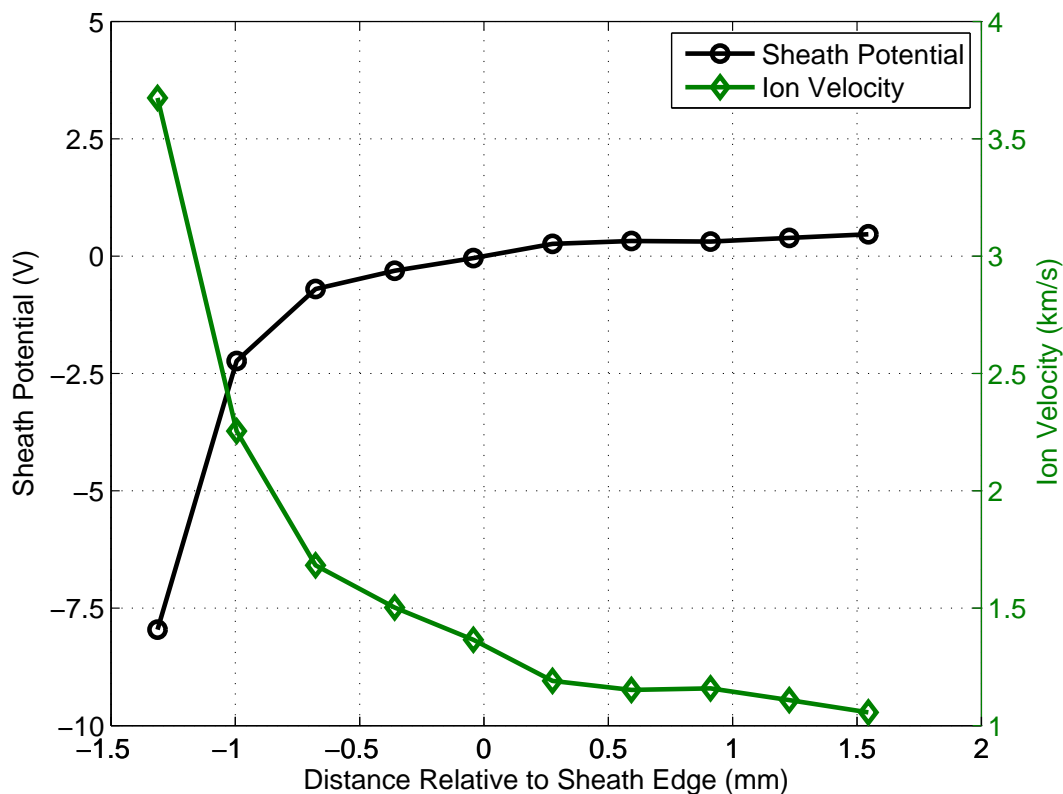


**Figure 4.1:** Spatial profiles of the sheath potential and ion velocity as a function of relative distance from the sheath edge surrounding a molybdenum plate. Data shown in Figures 3.10 and 3.12 corresponds to the data point at  $-0.35$  mm. Plasma conditions are:  $n_{ep} = 2.2 \times 10^{16} \text{ m}^{-3}$ ,  $\alpha = 0.015$ ,  $T_{ep} = 2.5 \text{ eV}$ ,  $E_{pri} = 23 \text{ eV}$ ,  $\phi_p = 47 \text{ V}$ ,  $\phi_f = 31 \text{ V}$ ,  $u_B = 1300 \text{ m/s}$ ,  $\lambda_D = 79 \text{ }\mu\text{m}$ .

cm and immeasurable from a practical standpoint and due to the limited travel of collection stage and size of the optics.

Typical values of the 95% confidence interval resulting from the Gaussian LIF fit range from 0.01 to 0.03 GHz on both LIF peaks, and generally increases with the depth of measurement in the sheath. With a typical maximum confidence interval of 0.03 GHz, and therefore 0.06 GHz on the peak separation, translates to a ion velocity of  $\sim 25$  m/s. This is a negligible amount of error and is not displayed in Figure 4.1 or any of the following sheath profiles.

Assuming the sheath edge is located where the ions achieve the Bohm velocity and this location is at the plasma potential (ignoring presheath) found using a Langmuir probe, the Child-Langmuir model estimates the sheath thickness to be  $245 \mu\text{m}$  using Equation 1.10. This estimate is considerably smaller than the 1.3 mm of measurable sheath via LIF shown in Figure 4.1 and is most likely attributed to the incorrect application of this model. The Child-Langmuir model requires  $e\phi_s \gg kT_e$ , and an analysis of the Langmuir probe I-V data from a typical plasma (this test being no exception), including the numerical analysis, results in  $e\phi_s/kT_e \approx 5$ , which is not high enough to ignore the presheath or electron influence in the sheath. Other quantities and parameters will have to be used in order to characterize measured sheath profiles.

Using Equation 1.8 given again as

$$n_i(x) = n_0 \left( 1 - \frac{2e\phi(x)}{Mu_B^2} \right)^{-1/2}, \quad (4.1)$$

where  $\phi(-1.35) = -7.96$  V and assuming quasineutrality at the sheath edge, ion density  $n_0$  is equal to the measured electron density  $n_{ep} = 2.2 \times 10^{16} \text{ m}^{-3}$ , the ion density at the last measurement location is  $n_i(-1.35) = 7.8 \times 10^{15} \text{ m}^{-3}$ . This estimated density is  $\sim 35\%$  of the plasma density. The projected ion density at the sheath-wall boundary where  $\phi(x) = -16 = \phi_f - \phi_p$  is  $5.7 \times 10^{15} \text{ m}^{-3}$ , and is  $\sim 26\%$  of the plasma density.

## 4.2 Repeatability Test

To test the repeatability of this diagnostic technique, sheaths surrounding molybdenum at three different biases were each measured twice. The molybdenum plate was biased at +/- 10 V with respect to floating and forced at floating. Forcing the plate to a voltage where the current is zero with a power supply, is to ensure the sheath characteristics remain as constant as possible throughout the ~4 hour test, as the plasma invariably changes slightly. If this were not done, the floating potential would change about about 1 V over the same time period, causing the ion velocity to also change. The six tests were conducted over a period of 3 days, each with their own slightly different plasma parameters listed in Table 4.1. Despite the slight variation in plasma conditions, the plasma source was operated at the same current and voltages that maintain the plasma.

Using Equation 4.1 and making the same assumptions as previously discussed in section 4.1, the estimated ion density at the last measurable location is shown in Figure 4.2 along with the sheath potential profiles. As expected, a lower wall potential forces the sheath voltage to be greater, causing greater ion velocities and thicker sheaths. The Child-Langmuir law may be invalid to apply quantitatively, but qualitatively, it states that the sheath thickness increases with the Debye length and the sheath voltage. Consequently, the sheath profiles of the +10 V biased case represent a larger percentage of the entire sheath compared to the profiles of the other two biases. It is possible the +10 V sheaths were measured up to the

**Table 4.1: Plasma conditions obtained from the Langmuir probe for each of the three plasma types denoted in Figure 4.2, where  $\alpha = n_{pri}/(n_{ep}+n_{pri})$ . Values are dimensionless or given in SI units except the electron temperatures and Debye length which are given in eV and  $\mu m$ , respectively.**

Plasma	$n_{ep}$	$n_{pri}$	$\alpha$	$T_{ep}$	$E_{pri}$	$\phi_p$	$\phi_f$	$u_B$	$\lambda_D$
1	$1.8 \times 10^{16}$	$2.2 \times 10^{14}$	0.012	2.7	22	41	26	1400	91
2	$3.0 \times 10^{16}$	$2.8 \times 10^{14}$	0.0092	2.6	23	41	24	1400	69
3	$2.4 \times 10^{16}$	$2.4 \times 10^{14}$	0.0099	2.7	25	41	24	1400	78

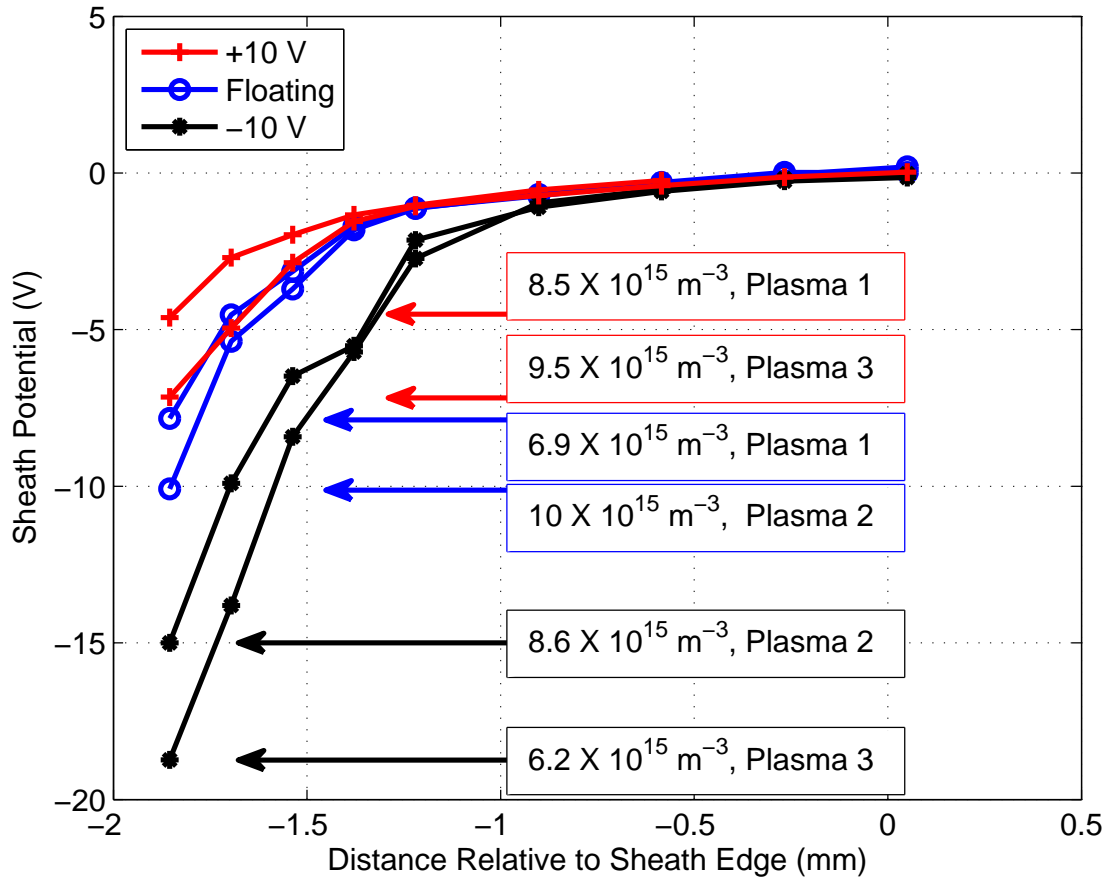


Figure 4.2: Spatial potential profiles of sheaths surrounding biased molybdenum (+/- 10 volts with respect to floating potential and forced floating) with two tests per bias, all under similar plasma conditions. The plot annotations denote the approximate final ion density at the last measurement point and the respective plasma type for which the conditions are listed in Table 4.1.

wall or at least very close, due to the expected sheath voltage of 5 V and 7 V for the #1 and #3 plasma respectively. However, there is no way to verify with another method. The 2 V difference in sheath voltage between plasma #1 and #2, also explains the difference in ending potential between the two floating cases. As for the two -10 V cases, there appears to be no correlation between the plasma conditions and the difference in ending potentials.

Ion density being the most probable determining factor of where the ending measurement point occurs, one would expect the density to be somewhat constant among each of the six ending points. Perhaps the cause of the variation in ending plasma density is a combination

of the measurement error in the Langmuir probe and the differences in laser power from test to test. Regardless, the -10 V bias test that reached an ending potential of -18.7 V marks the lowest measureable density and the greatest change in density, with a reduction of  $\sim 75\%$  with respect to the sheath edge.

### 4.3 Wall Material Effect

To determine the effect of two common Hall thruster channel wall materials on plasma sheaths, tests were ran using alumina ( $Al_2O_3$ ) and boron nitride ( $BN$ ) each at two different discharge currents ( $I_D$ ). Plasma conditions obtained from the Langmuir probe and sheath voltage  $\phi_s$  and SEE yield  $\gamma$  resulting from the numerical analysis in Chapter 2 for each of the four tests are given in Table 4.2. All operating parameters (xenon flow rate, current/voltage of filament, PBN, grid, etc.) were held constant except the test material type, and discharge current. The operating conditions were: xenon flow rate of 1 sccm, 8 A filament, 10 V at the PBN (accounting for voltage drop across ballast resistor) and -15 V grid. Figure 4.3 shows the measured sheath profiles for each test case, focusing on the region of sheath this technique is capable of measuring including some of the presheath (with the exception of the alumina at 0.8 A case where the sheath edge was extrapolated).

All the parameters shown in Table 4.2 affect the sheath characteristics. As discussed in Chapters 1 and 2: the plasma potential  $\phi_p$  affects the local potential at the sheath-presheath

**Table 4.2: Plasma conditions obtained from the Langmuir probe at each of the four tests. Sheath voltage  $\phi_s$  and SEE yield  $\gamma$  were determined from simulation. Values are dimensionless or given in SI units except the electron temperatures and Debye length which are given in  $eV$  and  $\mu m$ , respectively.**

Material/ $I_D$	$n_{ep}$	$n_{pri}$	$\alpha$	$T_{ep}$	$E_{pri}$	$\phi_p$	$\phi_f$	$u_B$	$\lambda_D$	$\phi_s$	$\gamma$
$Al_2O_3/0.8$ A	$2.8 \times 10^{16}$	$1.7 \times 10^{15}$	0.057	3.2	16	34	16	1500	82	16.4	0.058
$BN/0.8$ A	$2.4 \times 10^{16}$	$1.6 \times 10^{15}$	0.061	3.1	16	33	16	1500	82	15.9	0.065
$Al_2O_3/1.6$ A	$5.9 \times 10^{16}$	$2.1 \times 10^{15}$	0.034	3.1	22	37	20	1500	53	15.9	0.081
$BN/1.6$ A	$5.8 \times 10^{16}$	$2.0 \times 10^{15}$	0.033	3.1	21	37	19	1500	53	15.7	0.079

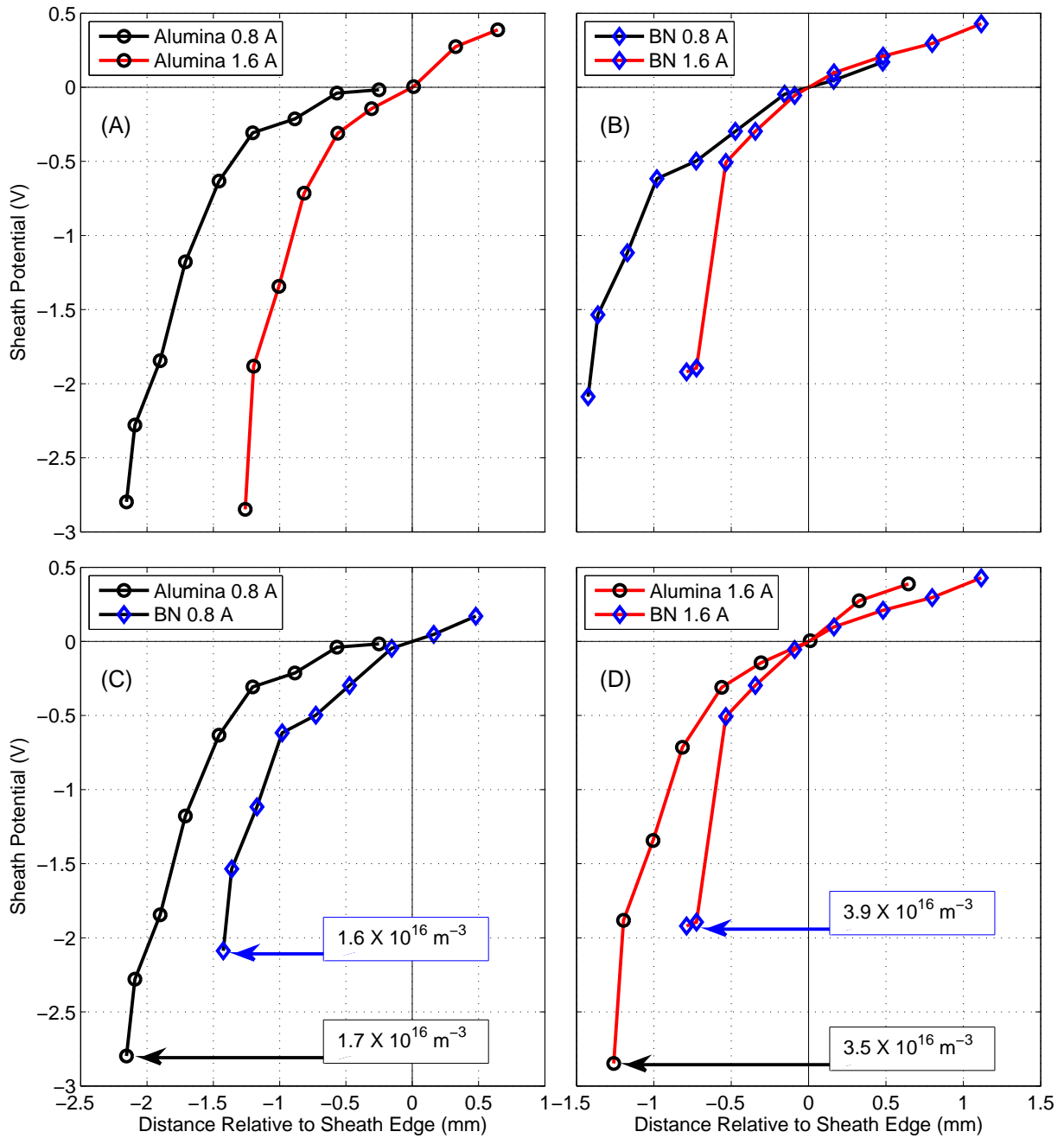


Figure 4.3: Four sheath profiles surrounding wall materials alumina and BN at 0.8 A and 1.6 A discharge current plotted two different ways for comparison. (A) and (B): similar materials compared at dissimilar plasma conditions. (C) and (D): dissimilar materials compared at similar plasma conditions. Annotations on (C) and (D) indicate the estimated ion density at the last measured data point.

boundary, the electron temperature affects the sheath voltage  $\phi_s$  and Bohm velocity  $u_B$ , and many parameters affect the floating wall potential  $\phi_f$ , which is the potential at the plasma-wall boundary (although evidence suggests this potential is different from the last measurable point in these tests), and is directly related to the sheath voltage.

As expected, the higher plasma potential at the discharge current of 1.6 A causes a higher local potential at the sheath-presheath boundary. This cannot be determined from the sheath profile graphs, but can be determined knowing the ions must experience a potential drop of at least  $kT_{ep}/(2e)$  to reach the Bohm velocity. Because electron temperature is independent of discharge current (ignoring the small variation in  $T_{ep}$  between alumina at 0.8 A and the other tests), the minimum potential drop across the presheath is the same for all four tests and therefore a higher local potential at the sheath-presheath boundary exists for the 1.6 A cases. For example, the sheath-presheath boundary is at approximately 32 and 35 volts for the 0.8 and 1.6 A tests, given a minimum presheath voltage of  $\sim 2$  V.

The primary electron density is roughly 3-6% of the total electron density and because filament bias voltage was held constant, the energy is linearly related to the plasma potential. Recall that primary electrons have an energy equal to the potential difference between the filament and plasma potential and cannot be directly used to obtain a SEE yield. According to the simulation, the sheath voltage is  $\sim 16$  V for all four cases, which means only electrons of energy greater than  $\phi_s$  can impact the wall. The effect of primary electrons at low energy and density fraction is small but not necessarily negligible as discussed in Chapter 2.

According to Equations 1.15 and 1.16, the Hobbs and Wesson<sup>28</sup> theory of an emissive sheath estimates the critical SEE yield  $\gamma_{cr}$  for a xenon plasma is  $\sim 0.983$  resulting in a  $\phi_s \approx 3.16$  V at  $T_{ep} = 3.1$  eV. At this point, the sheath is in the space-charge-limited regime and the result is a change in direction of the electric field causing a virtual cathode near the wall. The comparatively much smaller values of  $\phi_s$  and  $\gamma$  from simulation in Table 4.2 indicate the sheaths in all the four test cases are not space-charge-limited by secondary electrons and will be monotonic. This, however, does not provide an explanation for the

last two data points for the BN 1.6 A case, which indicate a near zero electric field at that location. The secondary electrons do play a role in reducing the sheath voltage, but with the calculated SEE yield ranging from  $\sim 0.08$  to  $0.06$  the effect is not great enough to cause anything of interest. Shown in Table 4.3 is the simulated difference in sheath voltage for the four cases with expected SEE and without SEE. The influence of secondary electrons reduces the sheath voltage by about 0.20-0.30 volts which is  $\sim 1-2\%$  of the initial value. Therefore, these wall material tests are minimally affected by SEE and the effect can be neglected. The discharge is capable of generating a plasma with high energy electrons ( $\sim 50$  eV primaries) to induce more SEE, but the plasma is much more energetic causing everything inside to be quickly sputter coated with metal, including the ceramic.

The ending ion density is very similar for both  $I_D = 0.8$  A cases and the difference in ending potential is a consequence of the slightly different plasma density, allowing the alumina 0.8 A case a higher density deeper into the sheath. In addition, all of the ending densities constitute  $\sim 60\%$  of the initial density. Although, the reason for why the alumina 0.8 A data is offset by  $\sim 0.5$  mm compared to BN 0.8 A for nearly all points is unknown. Results from simulation and Langmuir probe suggest the two sheaths should be very similar. This offset could be a result of the extrapolation (to zero it with respect to sheath edge) error and/or incorrect determination of the sheath edge location.

**Table 4.3: Comparing sheath voltage  $\phi_s$  determined from simulation when SEE is non-existent ( $\gamma = 0$ ), and as expected ( $\gamma$  listed in Table 4.2).**

Material/ $I_D$	$\phi_s$ Without SEE	$\phi_s$ With SEE	$\Delta\phi_s$
$Al_2O_3/0.8$ A	16.6	16.4	0.20
$BN/0.8$ A	16.1	15.9	0.20
$Al_2O_3/1.6$ A	16.2	15.9	0.30
$BN/1.6$ A	16.0	15.7	0.30

When comparing the sheath profiles surrounding the ceramics in Figure 4.3 with Figures 4.1 and 4.2 which are both from molybdenum, the significant difference is the higher ending density. This is most likely due to the semi-polished molybdenum providing a much better reflection and therefore a stronger, more narrow redshifted signal, which lowers the density detection limit and allows deeper sheath measurements.

In hindsight, setting up the imaging optics to magnify the image by 2x onto the monochromator may have been an unwise decision which negatively affected the SNR without a practical benefit. A spatial resolution of 60 microns is simply too small to take advantage of, given the length of time it takes to measure an entire sheath. If a 2 mm thick sheath was measured every 60 microns, ignoring the presheath, it would take about 15 hours for 33 measurements with two scans each, accounting for the plasma warm up procedure and the constant adjustment of the laser. The above profiles contain 9-10 measurement points per sheath, which is a good balance between reliably being able to get the data in one day and measuring as many points in the sheath to accurately capture it. By extension, this causes the actual resolution of the measurement points to be much greater than 60 microns. Conceivably, with half the LIF power reaching the detector due to magnification, this increases the minimum detectable density by a factor of two and limits the depth of measurement. For example, the projected ion density at -15 V below the sheath edge of the alumina 0.8 A test is  $8.5 \times 10^{15} \text{ m}^{-3}$  which is exactly half the estimated density at the last measured point. According to the numerical analysis the sheath voltage of this case is 16.4 V which means, if the minimum detectable density was halved, the last measurement point would have been very close to the wall. However, increasing the spatial resolution would sample a larger volume, further Doppler broaden the LIF signal and may not increase the LIF signal advantageously. Therefore, it is unknown whether or not doubling the spatial resolution would increase the depth of measurement.

## 5 Conclusion and Future Work

### 5.1 Conclusion

This thesis presented the advancement of a laser diagnostic technique to study plasma-wall interactions. Significant experimental advancements were made to enable the ability of spatially resolved sheath potential profiles. Improvements were made to boost the collection efficiency, LIF power, optimize the signal processing and reduce the noise which collectively increased the signal-to-noise ratio by a factor of  $\sim 200$ . A numerical analysis was also conducted to show the separate influence of primary electron energy and density fraction on SEE yield and sheath voltage. It was a theoretical analysis specific to the measured plasma conditions to compare against experimental results and further understand the complexity of plasma-wall interactions.

In conclusion, LIF is a powerful measurement technique for probing ion velocity in a plasma sheath, but it presents its own difficulties. Currently, measurements are limited to sheaths causing no more than a 75% reduction in the ion density for good reflectors such as molybdenum and  $\sim 40\%$  for poor reflectors such as ceramics. More work is required to lower the minimum detectable density in sheaths surrounding ceramics to measure the expected maximum velocity.

### 5.2 Future Work

Being that a significant limitation of this experiment is the indeterminate location of the measurements, an ideal next step is to attempt to solve, or at least mitigate it as much as possible. The underlying issue is opening the chamber and switching out materials invariably moves the location of the test piece along the beam path, however minute. Knowing the precise location of the measurements with respect to the wall would vastly improve the significance of the data. With a metal test piece mounted in the plasma source, one can bias it to the plasma potential. Assuming no present space charge effects from secondary electrons, this would theoretically eliminate the sheath, ion density would remain constant and allow

ample signal strength up to the wall. If LIF could be detected immediately up to a surface, it would provide an accurate location of the wall, within some error governed by the amount of tilt of the wall towards the collection optics and the width of the beam. A device that could index between metal test piece and others of interest (alumina, BN, etc.) to a precise position while the plasma source is running would provide a way to accurately determine the sheath thickness surrounding a ceramic wall, regardless of the plasma condition.

Other experimental improvements that would aid in the researching of plasma sheaths include:

- Lower operating pressure. A xenon plasma with fewer contaminate ions will produce a sheath that is more representative of the conditions found in an operating Hall thruster in space.
- A scaled experiment. Using larger components such as a chamber, plasma source, windows and collection optics would allow for more pump power and a higher collection efficiency.
- A more advanced laser (such as Toptica DL pro or TA pro). One that is capable of operating longer while scanning larger ranges.

## References

- [1] Taccogna, F.; Longo, S.; Capitelli, M.; Schneider, R. Anomalous transport induced by sheath instability in Hall effect thrusters. *Applied Physics Letters* **2009**, *94*, 20–24.
- [2] Goebel, D. M.; Katz, I. Fundamentals of Electric Propulsion: Ion and Hall Thrusters. In *Fundamentals of Electric Propulsion: Ion and Hall Thrusters*; JPL Space Science And Technology Series; Wiley: New York, 2008; pp 1–507.
- [3] Taccogna, F. Non-classical plasma sheaths: space-charge-limited and inverse regimes under strong emission from surfaces. *The European Physical Journal D* **2014**, *68*, 199.
- [4] Schinder, A. M.; Walker, M.; Rimoli, J. J. Three-Dimensional Model for Erosion of a Hall-Effect Thruster Discharge Channel Wall. *Journal of Propulsion and Power* **2014**, *30*, 1373–1382.
- [5] Mikellides, I.; Katz, I.; Hofer, R.; Goebel, D.; de Grys, K.; Mathers, A. Magnetic Shielding of the Acceleration Channel Walls in a Long-Life Hall Thruster. 46th AIAA/ASME/SAE/ASEE Joint Propulsion Conference & Exhibit. 2010.
- [6] de Grys, K.; Mathers, A.; Welander, B.; Khayms, V. Demonstration of 10,400 Hours of Operation on 4.5 kW Qualification Model Hall Thruster. In *46th AIAA/ASME/SAE/ASEE Joint Propulsion Conference & Exhibit*; Joint Propulsion Conferences; American Institute of Aeronautics and Astronautics, 2010.
- [7] Hofer, R. R.; Jorns, B. A.; Polk, J. E.; Mikellides, I. G.; Snyder, J. S. Wear test of a magnetically shielded Hall thruster at 3000 seconds specific impulse. *33rd International Electric Propulsion Conference* **2013**,
- [8] Chen, F. F. *Introduction to Plasma Physics and Controlled Fusion*; Springer, 1983; Vol. 1.
- [9] Callen, J. Collective Plasma Phenomena. In *Fundamentals of Plasma Physics*, draft ed.; 2003; Chapter 1.
- [10] Lee, D.; Hershkowitz, N.; Severn, G. D. Measurements of Ar<sup>+</sup> and Xe<sup>+</sup> velocities near the sheath boundary of Ar-Xe plasma using two diode lasers. *Applied Physics Letters* **2007**, *91*, 041505.
- [11] Bohm, D. The Characteristics of Electrical Discharges in Magnetic Fields. In *The Characteristics of Electrical Discharges in Magnetic Fields*; Guthrie, A., Wakerling, R. K., Eds.; McGraw-Hill: New York, 1949; Chapter Chapter 1, p 77.
- [12] Chen, F. F. Electric Probes. In *Plasma Diagnostic Techniques*, 1st ed.; Huddlestone, R. H., Leonard, S. L., Eds.; Academic Press: New York, 1965; Chapter 3, pp 113–200.
- [13] Tonks, L.; Langmuir, I. A general theory of the plasma of an arc. *Physical Review* **1929**, *34*, 876–922.

- [14] Lieberman, M. A.; Lichtenberg, A. J. *Principles of Plasma Discharges and Materials Processing*; Wiley, 2005.
- [15] Sheridan, T. E.; Goree, J. A. Analytic Expression For The Electric Potential In The Plasma Sheath. *IEEE Transactions on Plasma Science* **1989**, *17*, 884–888.
- [16] Severn, G. D.; Wang, X.; Ko, E.; Hershkowitz, N. Experimental Studies of the Bohm Criterion in a Two-Ion-Species Plasma Using Laser-Induced Fluorescence. *Phys. Rev. Lett.* **2003**, *90*, 145001.
- [17] Child, C. D. Discharge from hot CaO. *Physical Review (Series I)* **1911**, *32*, 492–511.
- [18] Langmuir, I. The effect of space charge and residual gases on thermionic currents in high vacuum. *Physical Review* **1913**, *2*, 450–486.
- [19] Sheehan, J. The Effects of Space-Charge Limited Electron Emission on the Plasma Sheath. Ph.D. thesis, The University of Wisconsin - Madison, 2012.
- [20] Gascon, N.; Dudeck, M.; Barral, S. Wall material effects in stationary plasma thrusters. I. Parametric studies of an SPT-100. *Physics of Plasmas* **2003**, *10*, 4123–4136.
- [21] Hall, L. S.; Bernstein, I. *Modification of the Electrostatic Sheath By Secondary Emission of Electrons*; 1976.
- [22] Robertson, S. Sheaths in laboratory and space plasmas. *Plasma Physics and Controlled Fusion* **2013**, *55*, 093001.
- [23] Patino, M. I.; Raiteses, Y.; Koel, B. E.; Wirz, R. E. Analysis of secondary electron emission for conducting materials using 4-grid LEED/AES optics. *Journal of Physics D: Applied Physics* **2015**, *48*, 195204.
- [24] Seiler, H. Secondary electron emission in the scanning electron microscope. *Journal of Applied Physics* **1983**, *54*.
- [25] Sydorenko, D.; Kaganovich, I.; Raiteses, Y.; Smolyakov, A. Breakdown of a space charge limited regime of a sheath in a weakly collisional plasma bounded by walls with secondary electron emission. *Physical Review Letters* **2009**, *103*, 145004.
- [26] Campanell, M. D.; Khrabrov, A. V.; Kaganovich, I. D. Absence of debye sheaths due to secondary electron emission. *Physical Review Letters* **2012**, *108*, 255001.
- [27] Schweigert, I. V.; Langendorf, S. J.; Walker, M. L. R.; Keidar, M. Sheath structure transition controlled by secondary electron emission. *Plasma Sources Science and Technology* **2015**, *24*, 025012.
- [28] Hobbs, G. D.; Wesson, J. A. Heat flow through a Langmuir sheath in the presence of electron emission. *Plasma Physics* **1967**, *9*, 85–87.

- [29] Seon, J.; Lee, E.; Choe, W.; Lee, H. J. One-dimensional solution to the stable, space-charge-limited emission of secondary electrons from plasma-wall interactions. *Current Applied Physics* **2012**, *12*, 663–667.
- [30] Seon, J.; Lee, E. Plasma Wall Potentials with Secondary Electron Emissions up to the Stable Space-Charge-Limited Condition. *Plasma Science and Technology* **2013**, *15*, 1093–1099.
- [31] Langendorf, S.; Walker, M. Effect of secondary electron emission on the plasma sheath. *Physics of Plasmas* **2015**, *22*, 033515.
- [32] Gallimore, A.; Wang, L. An Investigation of Plasma-Wall Interactions in Plasma Propulsion Systems. 2011.
- [33] Langmuir, I. The Interaction of Electron and Positive Ion Space Charges in Cathode Sheaths. *Phys. Rev.* **1929**, *33*, 954–989.
- [34] Andrews, J. G.; Allen, J. E. Theory of a Double Sheath between Two Plasmas. *Proceedings of the Royal Society of London A: Mathematical, Physical and Engineering Sciences* **1971**, *320*, 459–472.
- [35] Campanell, M. D.; Khrabrov, A. V.; Kaganovich, I. D. General cause of sheath instability identified for low collisionality plasmas in devices with secondary electron emission. *Physical Review Letters* **2012**, *108*, 235001.
- [36] Campanell, M. D. Negative plasma potential relative to electron-emitting surfaces. *Physical Review E - Statistical, Nonlinear, and Soft Matter Physics* **2013**, *88*, 1–10.
- [37] Sydorenko, D.; Smolyakov, A.; Kaganovich, I.; Raiteses, Y. Modification of electron velocity distribution in bounded plasmas by secondary electron emission. *IEEE Transactions on Plasma Science* **2006**, *34*, 815–824.
- [38] Kaganovich, I. D.; Raiteses, Y.; Sydorenko, D.; Smolyakov, A. Kinetic effects in a Hall thruster discharge. *Physics of Plasmas* **2007**, *14*, 057104.
- [39] Raiteses, Y.; Staack, D.; Keidar, M.; Fisch, N. J. Electron-wall interaction in Hall thrusters. *Physics of Plasmas* **2005**, *12*, 1–7.
- [40] Gascon, N.; Thomas, C. A.; Hermann, W. A.; Cappelli, M. A. Operating regimes of a linear SPT with low secondary electron-induced wall conductivity. AIAA Joint Propulsion Conference. 2003; pp 1–8.
- [41] Ahedo, E.; Gallardo, J. M.; Martínez-Sánchez, M. Effects of the radial plasma-wall interaction on the Hall thruster discharge. *Physics of Plasmas* **2003**, *10*, 3397–3409.
- [42] Barral, S.; Makowski, K.; Peradzyński, Z.; Gascon, N.; Dudeck, M. Wall material effects in stationary plasma thrusters. II. Near-wall and in-wall conductivity. *Physics of Plasmas* **2003**, *10*, 4137–4152.

- [43] Keidar, M.; Boyd, I. D.; Beilis, I. I. Plasma flow and plasma-wall transition in Hall thruster channel. *Physics of Plasmas* **2001**, *8*, 5315–5322.
- [44] Taccogna, F.; Schneider, R.; Longo, S.; Capitelli, M. Kinetic simulations of a plasma thruster. *Plasma Sources Science and Technology* **2008**, *17*, 024003.
- [45] Meezan, N. B.; Cappelli, M. A. Kinetic study of wall collisions in a coaxial hall discharge. *Physical Review E - Statistical, Nonlinear, and Soft Matter Physics* **2002**, *66*, 36401.
- [46] Mott-Smith, H. M.; Langmuir, I. The theory of collectors in gaseous discharges. *Physical Review* **1926**, *28*, 727–763.
- [47] Auciello, O.; Flamm, D. L. How Langmuir Probes Work. In *Plasma Diagnostics: Discharge Parameters and Chemistry*; Academic Press: New York, 1989; pp 113–183.
- [48] Hershkowitz, N. Sheaths: More complicated than you think. *Physics of Plasmas* **2005**, *12*, 1–11.
- [49] Reid, B.; Shastry, R.; Gallimore, A.; Hofer, R. Angularly-Resolved ExB Probe Spectra in the Plume of a 6-kW Hall Thruster. In *44th AIAA/ASME/SAE/ASEE Joint Propulsion Conference & Exhibit*; Joint Propulsion Conferences; American Institute of Aeronautics and Astronautics, 2008.
- [50] Yamada, H.; Murphree, D. L. Electrostatic Probe Measurements in a Collisionless Plasma Sheath. *Physics of Fluids* **1971**, *14*.
- [51] Oksuz, L.; Hershkowitz, N. First Experimental Measurements of the Plasma Potential throughout the Presheath and Sheath at a Boundary in a Weakly Collisional Plasma. *Phys. Rev. Lett.* **2002**, *89*, 145001.
- [52] Donnelly, V. M.; Flamm, D. L.; Collins, G. Laser diagnostics of plasma etching: Measurement of Cl+2 in a chlorine discharge. *Journal of Vacuum Science & Technology* **1982**, *21*.
- [53] Gottscho, R. A.; Mandich, M. L. Time-resolved optical diagnostics of radio frequency plasmas. *Journal of Vacuum Science & Technology A* **1985**, *3*.
- [54] Goeckner, M. J.; Goree, J.; Sheridan, T. E. Measurements of ion velocity and density in the plasma sheath. *Physics of Fluids B* **1992**, *4*, 1663–1670.
- [55] Lam, S. W.; Hershkowitz, N. A new ion pitch-angle diagnostic for magnetized plasmas. *Plasma Sources Science and Technology* **1994**, *3*, 40.
- [56] Lee, D.; Severn, G.; Oksuz, L.; Hershkowitz, N. Laser-induced fluorescence measurements of argon ion velocities near the sheath boundary of an argonxenon plasma. *Journal of Physics D: Applied Physics* **2006**, *39*, 5230.
- [57] Lee, D.; Hershkowitz, N.; Severn, G. Experimental studies of transverse metastable ion velocity distribution functions in the presheath of a weakly collisional argon plasma. *Physics of Plasmas* **2008**, *15*.

- [58] Oksuz, L.; Khedr, M. A.; Hershkowitz, N. Laser induced fluorescence of argon ions in a plasma presheath. *Physics of Plasmas* **2001**, *8*.
- [59] Severn, G. D.; Wang, X.; Ko, E.; Hershkowitz, N.; Turner, M. M.; McWilliams, R. Ion flow and sheath physics studies in multiple ion species plasmas using diode laser based laser-induced fluorescence. *Thin Solid Films* **2006**, *506507*, 674–678.
- [60] Severn, G.; Lee, D.; Hershkowitz, N. Xenon ion laser-induced fluorescence using a visible tunable diode laser near 680nm. *Review of Scientific Instruments* **2007**, *78*.
- [61] Severn, G.; Yip, C. S.; Hershkowitz, N. Measurements of the ion drift velocities in the presheaths of plasmas with multiple ion species. *Journal of Instrumentation* **2013**, *8*, C11020.
- [62] Woo, H. J.; Chung, K. S.; Lho, T. H.; McWilliams, R. A newly calibrated laser-induced fluorescence(LIF) system for Ar ions with a single tunable diode laser. *Journal of the Korean Physical Society* **2006**, *48*, 260–265.
- [63] Keesee, A. M.; Scime, E. E.; Boivin, R. F. Laser-induced fluorescence measurements of three plasma species with a tunable diode laser. *Review of Scientific Instruments* **2004**, *75*.
- [64] Biloiu, I. A.; Scime, E. E. Ion acceleration in ArXe and ArHe plasmas. II. Ion velocity distribution functions. *Physics of Plasmas* **2010**, *17*.
- [65] Durot, C. J.; Gallimore, A. D.; Smith, T. B. Validation and evaluation of a novel time-resolved laser-induced fluorescence technique. *Review of Scientific Instruments* **2014**, *85*, 013508.
- [66] Huang, W.; Gallimore, A. D.; Hofer, R. R. Neutral Flow Evolution in a Six-Kilowatt Hall Thruster. *Journal of Propulsion and Power* **2011**, *27*, 553–563.
- [67] Qing, S. W.; Li, H.; Wang, X. G.; Song, M. J.; Yu, D. R. Effect of anisotropic non-Maxwellian electron distribution function on plasma-wall interaction in Hall thrusters. *EPL (Europhysics Letters)* **2012**, *100*, 35002.
- [68] Cenian, A.; Rachubinski, H.; Chernukho, A.; Dudeck, M. Plasma-wall interactions in DC discharges and sheath of Langmuir probes. *European Physical Journal: Special Topics* **2013**, *222*, 2143–2156.
- [69] Callen, J. Plasma Descriptions I: Kinetic, Two-Fluid. In *Fundamentals of Plasma Physics*, draft ed.; 2003; Chapter 5.
- [70] Sheehan, J. P.; Hershkowitz, N.; Kaganovich, I. D.; Wang, H.; Raitses, Y.; Barnat, E. V.; Weatherford, B. R.; Sydorenko, D. Kinetic theory of plasma sheaths surrounding electron-emitting surfaces. *Physical Review Letters* **2013**, *111*, 1–5.
- [71] Sheehan, J. P.; Kaganovich, I. D.; Wang, H.; Sydorenko, D.; Raitses, Y.; Hershkowitz, N. Effects of emitted electron temperature on the plasma sheath. *Physics of Plasmas* **2014**, *21*.

- [72] Sydorenko, D.; Smolyakov, A.; Kaganovich, I.; Raitses, Y. Kinetic simulation of secondary electron emission effects in Hall thrusters. *Physics of Plasmas* **2006**, *13*, 1–4.
- [73] Langendorf, S. Effects of electron emission on plasma sheaths. PhD Thesis, Georgia Institute of Technology, 2015.
- [74] Dunaevsky, A.; Raitses, Y.; Fisch, N. J. Secondary electron emission from dielectric materials of a Hall thruster with segmented electrodes. *Physics of Plasmas* **2003**, *10*, 2574–2577.
- [75] Zare, R. N. My Life with LIF: A Personal Account of Developing Laser-Induced Fluorescence. *Annual Review of Analytical Chemistry* **2012**, *5*, 1–14.
- [76] Bourgeois, G.; Mazouffre, S.; Sadeghi, N. Unexpected transverse velocity component of Xe<sup>+</sup> ions near the exit plane of a Hall thruster. *Physics of Plasmas* **2010**, *17*, 113502.
- [77] Huang, W.; Reid, B. M.; Smith, T. B.; Gallimore, A. D. Laser-Induced Fluorescence of Singly-Charged Xenon in a 6-kW Hall Thruster Plume. AIAA Joint Propulsion Conference. 2008; pp 1–14.
- [78] Liebeskind, J. G.; Hanson, R. K.; Cappelli, M. a. Laser-induced fluorescence diagnostic for temperature and velocity measurements in a hydrogen arcjet plume. *Applied Optics* **1993**, *32*, 6117–27.
- [79] Czarnetzki, U.; Luggenhölscher, D.; Döbele, H. F. Space and time resolved electric field measurements in helium and hydrogen RF-discharges. *Plasma Sources Science and Technology* **1999**, *8*, 230.
- [80] Merlino, R. L. Understanding Langmuir probe current-voltage characteristics. *American Journal of Physics* **2007**, *75*, 1078–1085.
- [81] Saloman, E. B. Energy Levels and Observed Spectral Lines of Xenon, Xe I through Xe LIV. *Journal of Physical and Chemical Reference Data* **2004**, *33*.
- [82] Bartlett, P. L.; Stelbovics, A. T. Calculation of electron-impact total-ionization cross sections. *Phys. Rev. A* **2002**, *66*, 12707.
- [83] Sawlani, K. U. Effects of Secondary Electron Emission on the Plasma Sheath and Local Electron Energy Distribution with Application to Hall Thrusters. Ph.D. thesis, The University of Michigan, 2015.
- [84] Huang, W. Study of Hall Thruster Discharge Channel Wall Erosion via Optical Diagnostics. Ph.D. thesis, University of Michigan, 2011.